Development and demonstration of a multiplexed magnetic tweezers assay

Keith Charles Johnson

A dissertation

submitted in partial fulfillment of the

requirements for the degree of

Doctor of Philosophy

University of Washington

2017

Reading Committee:

Wendy Thomas, Chair

Alberto Aliseda

Nathan Sniadecki

Program Authorized to Offer Degree:

Mechanical Engineering

© Copyright 2017

Keith Johnson

University of Washington

Abstract

Development and demonstration of a multiplexed magnetic tweezers assay

Keith Charles Johnson

Chair of the Supervisory Committee:
Associate Professor Wendy Thomas
Department of Bioengineering

This dissertation is concerned with the methods and applications of single molecule force spectroscopy. In the introduction, the traditional single molecule force spectroscopy instruments are introduced and the advantages and drawbacks of each are discussed. The first chapter is a review of methods to ensure that biomolecular bond lifetime parameter estimations are not contaminated by multiple bond data. This review culminates in an examination of the literature on the strength of the bond between biotin and streptavidin and finds that by filtering the numerous publications for those that clearly demonstrate specific single bond behavior, there is a consensus of the bond strength and kinetic parameters. The second chapter of the dissertation discusses the capabilities of a magnetic tweezer assay, which combines massive multiplexing, precision bead tracking, and bi-directional force control into a flexible and stabile platform for examining single molecule behavior. Using a novel method for increasing the precision of force estimations on heterogeneous paramagnetic beads, I demonstrate the instrument by examining the force dependence of uncoiling and recoiling velocity of type 1 fimbriae from *Eschericia coli* (*E. coli*) bacteria, and see similar results to previous studies. Chapter 3 is a study of the lifetime of the activated FimH-mannose bond under various force conditions using the previously described magnetic tweezer. The bond is found to be extremely long-lived at forces less than 30 pN, with an average lifetime > 1000 times longer than the biotin-streptavidin bond, making it one of the strongest non-covalent interactions known in nature. Furthermore, the average lifetime of the bond is similar between 9 and 30 pN of force, suggesting a force range at which the lifetime is force-independent, demonstrating ideal bond behavior for the first time in a natural system. It is hypothesized that the long lifetime and ideal behavior is due to a gateway that locks mannose into the binding pocket and opens at a rate independent of force. This study elucidates a mechanism for very strong biological binding, and provides insight into approaches for developing novel antiadhesive therapies. This dissertation is concluded with a review of the body of work in chapters 1-3 and a discussion of the future directions for this research.

Table of Contents

List of Figures

List of Tables

Acknowledgements

It would be remiss to not begin by thanking my adviser, Wendy Thomas. I have been very fortunate to have stumbled into her lab, and have learned a great deal under her guidance. Her brilliance, caring, and academic rigor have not only made me a better scientist, but inspired me to be a mentor myself.

I would like to thank all those in the Thomas Lab who I have worked with or alongside. In particular, I would like to thank Shivani Gupta, who has sat by me for the past six years. Her friendship has made coming to lab every day more enjoyable than it would have otherwise been. I'd also like to thank Olga Yakovenko and An-Yue Tu, the Queen and King of the Thomas Lab, for teaching me the ropes in the wet lab, and whose faces I will miss seeing every day.

My family, especially my parents, Terry and Lee Johnson, have been incredibly supportive of this long trek through grad school. They have also been a constant source of love and support in times of need, and for this I cannot thank them enough.

To my Seattle family of Colin Bateson, Lynne Matsuoka, and Alissa Bleem: the time I have spent with you has been some of the most rewarding of my life. Thank you so much for allowing me to be my truest self in your presence, and for loving me despite all my faults. Thank you also to the Domers who have showed me the true meaning of fun, the Dudes Book Club which has been a source of amazing conversations and comradery, the ageless wonder that is Roosevelt FC, and the Mudflingers with whom I have witnessed some of the greatest comebacks and victories of my life.

Lastly, I would like to thank Sheri Imsdahl, who inspired me to be a better person than I was when I arrived in graduate school.

Introduction

The goal of single molecule force spectroscopy (SMFS) experiments is to determine the force dependent properties of a biomolecular complex. Some applications include, but are not limited to, the determination the kinetics of biological bonds [1-3],viscoelastic cell properties [4], DNA stretching [5], and the characterization of motor proteins [6, 7]. The primary application in this document is the determination of biological binding kinetics, and therefore methodologies pertaining to such measurements will be discussed in more detail.

Biological adhesion plays an important role in maintaining homeostasis in the human body, such as the binding of Von Willebrand Factor (VWF) to platelets to initiate blood clotting at sites of injury [8], or leukocytes binding to blood vessel endothelial cells [9]. With the advent of SMFS, investigations of these phenomena have yielded powerful and valuable insights into the underlying behavior of biological bonds. The behavior of these bonds can also be pathogenic in nature: the binding of *Escherichia coli* (*E. coli*) to human tissues is the primary cause of urinary tract infections [10], and mutations in VWF can result in a bleeding disorder known as Von Willebrand Disease [8]. The recent discovery of an *E. coli* strain that is resistant to the antibiotic Colistin is a frightening reminder of the need for alternatives to antibiotics [11]. The understanding gained through the studies of these biological bonds has the potential to unlock novel therapies for adhesion based illnesses.

In a typical SMFS study of a biological bond, a probe is coated with a ligand/receptor, either through non-specific adsorption, covalent bonding, or other attachment techniques. Similarly, an opposing surface is coated with the complimentary ligand/receptor. The probe and surface can then be brought together to the point where the ligand and receptor can form a bond (Figure 1A).

By separating the surfaces at either constant velocity or force until bond rupture occurs, the lifetime of the bond can be determined as a function of force [12] (Figure 1B). By examining many bond ruptures at different forces or velocities, mathematical models [13, 14] can be fit to describe the kinetics of the bond. The traditional instruments used for SMFS are the Optical Tweezer (OT), Atomic Force Microscope (AFM), and Biomembrane Force Probe (BMFP).

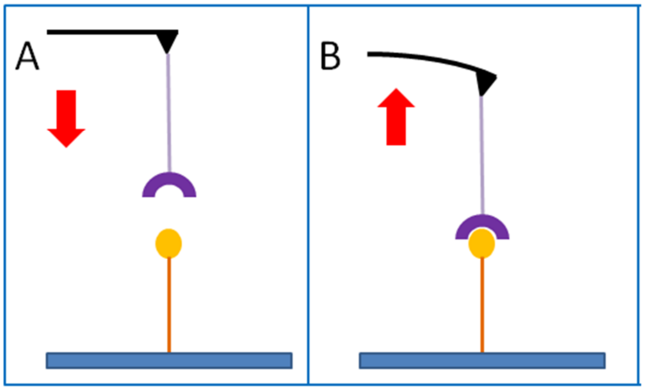

Figure 1: A.) Illustration of a probe approaching a surface allowing two biomolecules to interact. B.) After bond formation, the probe is retracted at either constant force or constant velocity until bond rupture.

Traditional Single Molecule Techniques

Optical Tweezers

In an optical tweezer or optical trap (OT) a particle is trapped at the focal point of a laser using a high NA microscope objective (Figure 2). When the particle is displaced from the focal point, it feels a restoring force that can be modeled as a linear spring. In this way, forces in the range of 0.1-100 pN can be obtained with spatial and temporal resolution on the order of nanometers and milliseconds, respectively [15].

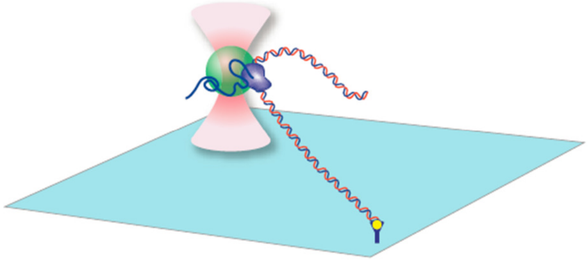

Figure 2: Cartoon of an Optical Trap assay. A particle is trapped at the focal point of a laser. Any displacement from the focal point results in a restoring force that can be modeled as a linear spring. Figure taken directly from Neumann and Nagy [15].

The OT is a robust and precise instrument; however it does have limitations and drawbacks. First, because a homogenous intensity distribution in the focal area is necessary for a precise trapping, any optical inhomogeneity in the medium will negatively affect the OT performance. The OT also will trap any freely diffusing objects in the medium, and thus samples with very low concentrations of objects of interest should be used to avoid capturing multiple objects simultaneously. The powerful lasers used to achieve the optical trap can also create local heating around the trapped object: a significant issue for any temperature dependent measurements, of which bond kinetics can be included.

Atomic Force Microscopy

Similar to that of the optical trap, in atomic force microscopy (AFM) a ligand coated probe is brought into contact with a receptor coated surface. However instead of the probe being an optically trapped particle, the probe for an AFM is a flexible cantilever, usually controlled by a piezo. The ligand coated tip of the cantilever is allowed to dwell at the surface allowing a bond to form, and then the cantilever is retracted in the vertical direction (Figure 1). If a bond does indeed form, it will prevent the tip of the cantilever from leaving the surface and thus act to bend the cantilever toward the surface. The deflection of the cantilever is measured via a laser reflecting off the top of the cantilever and onto a sensitive photodiode. With knowledge of the stiffness of the cantilever, and the deflection from the photodiode, the force on the cantilever tip can be determined. Using feedback control loops, the piezo can be used to control the amount of applied force, and thus provide constant force measurements. Using this method, force ranges of $10\text{-}10^4$ pN can be obtained [15].

While simple, and relatively easy to use, the AFM has drawbacks of its own. First, the stiff cantilevers create a low force resolution, preventing the precision of force measurements that can be obtained with other instruments. Secondly, knowing whether the measured adhesion was due to the bond of interest or non-specific interactions can be difficult to discern. This problem is amplified by the relatively high surface area of the cantilevers, which makes the likelihood of forming multiple adhesive interactions (specific or non-specific) greater [15]. Lastly, there can be significant cantilever drift over time, and thus maintaining a constant force over long periods can be challenging.

Biomembrane Force Probe

The biomembrane force probe (BMFP) uses a glass micropipette to control the displacement and stiffness of a biotinylated red blood cell (bRBC). By changing the aspiration pressure, the stiffness of the bRBC can be manipulated. A ligand coated bead is attached to the red blood cell and brought into contact with another bead (or cell) coated with complementary receptors, allowing one or more bonds to form (Figure 3). The beads are then separated and the bRBC monitored via video tracking to detect any elongation. Knowledge of the stiffness of the bRBC and the elongation yields the force between the beads [16].

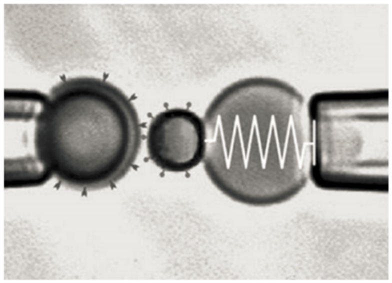

Figure 3: Picture of a biomembrane force probe. The stiffness of a red blood cell is controlled using aspiration pressure. By determining the elongation of the red blood cell, the force between the two beads can be determined. Figure taken directly from Gourier et al., [16].

The BMFP is one of the most robust systems in terms of force range (0.5-1000 pN) [17]. However, there are few commercially available systems to the author's knowledge, and thus the system must often be custom built. Also, it is very difficult to obtain constant force measurements with this setup because of the lack of a feedback loop to control the bRBC elongation. Thus, any measurements taken must be analyzed after the experiment, and the data usually binned into different force ranges. Lastly, the experimentation procedure can be time consuming and complex, making the BMFP perhaps the most cumbersome, but also most flexible SMFS system.

The Multiplexing Advantage

Perhaps the greatest challenge in gathering single molecule force data is the time it takes. As will be discussed later, ensuring single bonds often requires an adhesion rate of less than 0.2 [18], meaning that fully eighty percent of the measurements taken will not be useful. In addition, achieving statistically significant data can require several hundreds to thousands of measurements for a single force condition. Complex binding systems, where multiple constructs need to be examined at different forces, can thus be prohibitively costly to examine due to the time required to gather a sufficient amount of data.

Long bond lifetimes are particularly difficult to study using SMFS. For constant force measurements, the data acquisition time is proportional to the bond lifetime. If we consider a simple experiment measuring very short bond lifetimes, such that a lifetime measurement can be taken once every second, it would take 1000 seconds to examine 1000 lifetimes. But with an adhesion rate of 20% to ensure that the majority of attachments are single bonds, the measurement of 1000 lifetimes would require 5000 touches of the probe, and would therefore take 5000 seconds to gather the data. However, if we consider a long bond lifetime requiring a ten minute measurement, then gathering 1000 single molecule lifetimes would take ~35 days. Real time data analysis can reduce this time by eliminating the need for a full ten minute measurement when a bond does not form, but even under idealized circumstances this experiment would take a week of around the clock data acquisition. Again, this is for a single force, examining a single biological construct.

If multiple bonds could be probed simultaneously, this would reduce that data acquisition time and increase the scope of experiments that can be accomplished using SMFS. Unfortunately, the OT, AFM, and BMFP all take one measurement at a time. Luckily, there is an instrument that allows a high degree of multiplexing without sacrificing accuracy or precision in the measurements. This device is known as a magnetic tweezer and is described below.

The Magnetic Tweezer

Examining biological specimens using magnetic particles is a concept first developed in the 1950’s [19]. However, it was not until the 1990’s that the modern magnetic tweezer (MT) was developed and used to examine single molecules [20]. The MT is simple in design, and relatively inexpensive, but also has significant experimental advantages over other SMFS methods. At a base level, the MT consists of a magnet (either permanent or electromagnets) above a chamber situated on an inverted microscope (Figure 4). The magnetic field produced by this magnet tends to pull any magnetic particles towards the magnet. The chamber usually consists of paramagnetic beads suspended in a medium between two glass slides. The bottom slide can be coated with a ligand, and the magnetic beads with a corresponding receptor, or vice versa. The beads can be allowed to settle to the ligand coated surface, allowing bonds to form, and then the magnetic field is applied, pulling the beads away from the surface. In this way, a constant force can be applied to any bonds formed between the surface and bead. A high speed digital camera can be mounted to the microscope and takes images of the beads over time. As the beads move towards and away from the surface, their diffraction patterns will change, giving visual evidence of the relative position of the beads along the z-axis. Using these diffraction patterns, the three dimensional positions of the beads can be measured precisely, and used to determine any biomolecule extension or bond lifetimes.

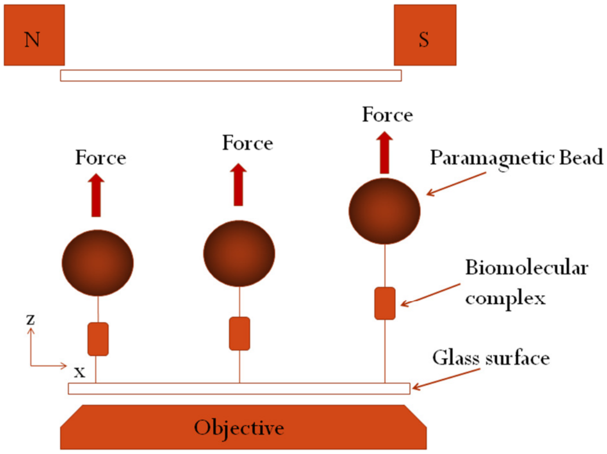

Figure 4: Illustration of a magnetic tweezers assay. A magnet above the chamber pulls beads away from the bottom surface at constant force. By examining the position of the beads, the force dependent properties of a biomolecular complex can be studied.

The greatest advantage of the MT is the ability to multiplex. All the beads in the field of view of the camera can be considered their own individual measurement, with each measurement being under essentially the same force. Thus, instead of examining one bond lifetime at a time, as is the case with the OT, AFM, and BMFP, tens and even hundreds of bond lifetimes can be measured simultaneously [21], drastically reducing the experimentation time needed to obtain statistically sufficient data.

The MMTB

In this dissertation, I expand the abilities of the magnetic tweezer by developing a multiplexed magnetic tweezer with precision bead tracking and bi-directional force control (MMTB). This instrument allows the simultaneous binding of up to 120 beads. Considering the example from above, I estimate that this will result in a 50% reduction in experimental time when measuring short bond lifetimes (1 s measurement) and an impressive 95% reduction in experimental time when measuring long bond lifetimes (10 minute measurement). I developed a bead tracking algorithm [22] that yields ≤ 10 nm of precision in all three dimensions, allowing the measurement of very short bond lifetimes and the detection of mechanical fingerprints [5]. I also added a magnet below the chamber such that force in both the upward and downward directions can be achieved. This lower magnet provides better contact time control of the beads with the lower surface, resulting in less non-specific adhesion, the ability to measure the kinetic on-rates, and improvement in the reproducibility of experiments. I further demonstrate the utility of the lower magnet by developing a novel method for force estimation on attached, heterogeneous beads that improves the precision of force estimates by 78%.

The first chapter of this dissertation is a review of methods to ensure that biomolecular bond lifetimes parameter estimations are not contaminated by multiple bond data. During this review, I recommend a set of criteria that can be used to ensure that the vast majority of measurements are of single bonds. Using these criteria, I reviewed the literature on the biotin-streptavidin bond and illustrate that those studies which meet the criteria show agreement as to strength and kinetic parameters of the bond. Perhaps the most important conclusion from this chapter is that the easiest way to ensure single molecule measurements is by reducing the fraction of touches that result in bond formation. This, of course, means that many touches will be needed, further demonstrating the need for a high throughput instrument such as the newly developed MMTB.

In the second chapter, I discuss the MMTB in detail, emphasizing the methods used for calibration, data acquisition, and data analysis. I also discuss a novel method that combines density centrifugation and force correlation to increase the precision of force estimates of heterogeneous paramagnetic beads by 78% over stock beads. I then demonstrate the versatility of the instrument by measuring the uncoiling and recoiling velocities of type 1 fimbriae from *E. coli,* and find that the measurements are in relative agreement with measurements done by others using traditional SMFS techniques. I found that without the capabilities of multiplexing, precision bead tracking, and bidirectional force control, this experiment would have been significantly more difficult, thus illustrating the utility of the MMTB.

Finally, in Chapter 3, I conduct a study of the lifetime of the activated state of the FimH-mannose bond. This system is essential for the binding of bacteria to cells, the first step toward bacterial colonization that can result in urinary tract infections, which are becoming increasingly difficult to treat due to bacterial resistance [11]. I find that at low forces, the activated FimH-mannose bond has a very long average lifetime, greater than 1000 times as long as the biotin-streptavidin bond at similar forces. Furthermore, the average lifetime of the activated state is similar between 9 and 30 pN of force, suggesting a force range at which the lifetime is force-independent, demonstrating ideal bond behavior for the first time in a natural system. To provide further evidence for ideal bond behavior, I fit both a slip bond model and an ideal + slip bond model to the data, and find that only the ideal + slip model can explain the data. Finally, I hypothesize a four-state model to explain the data. The main feature of this model is a gateway that locks in the mannose, and acts independent of force resulting in the ideal behavior seen at low forces. Due to similarities in behavior between the FimH-mannose bond and other receptor-ligand bonds, the gateway mechanism of binding may be a ubiquitous solution for robust receptor-ligand binding in a variable flow environment. Understanding this mechanism of binding is important knowledge for developing novel antiadhesive therapeutics.

Chapter 1: Methods for ensuring single bonds using single molecule force spectroscopy

Abstract

With the advent of single molecule force spectroscopy (SMFS) it became possible to apply known forces to biomolecules in order to estimate bond and unfolding kinetics. Unfortunately, ensuring that force is being applied to only a single biomolecule can be difficult, requiring a diligence in experimental methods and data interpretation that can seem unnecessary. This review examines the different methodologies in the literature that are used to prevent data contamination by multiple molecule measurements. We then examine the literature concerning the strength of the bond between biotin and streptavidin and show that by filtering the numerous publications for those that clearly demonstrate specific single bond behavior, there is a consensus of the bond strength and kinetic parameters.

Introduction

Single molecule force spectroscopy (SMFS) has provided the means to examine force dependent properties of biomolecular complexes. Applications include but are not limited to the determination of biological bond lifetimes [1-3], viscoelastic cell properties [4], DNA stretching [5], and the characterization of motor proteins [6, 7]. One system which has been extensively studied is the bond between biotin and streptavidin, and the published results for the strength of this bond have been inconsistent [23]. For there to be disagreement about such a well-studied system is troubling, and begs the question of whether other SMFS investigations of less familiar systems can be trusted. It therefore seems that a standardization of methods would benefit the SMFS community at large.

One possible reason for the inconclusive results on the strength of the biotin-streptavidin bond is contamination of data from multiple bonds [23] since ensuring that measurements are due to single bond behavior can be difficult. There are many different methods that have been used to either reduce the effect of multiple bonds [12, 24], or to extract single bond characteristics from multiple bond data [25-27]. While the validity of some of these methods has been discussed [28], most of them have not, and therefore readers of these works are ill-prepared to judge the soundness of SMFS results.

Here we review the different methods for approaching the problem of multiple bond interactions. We break these methods into three categories. The first, Reducing Multiple Bonds, are those methods which attempt to reduce the amount of multiple molecule interactions. The second category, Single Bond Signatures, are methods which allow the discernment of single and multiple molecule attachments based on tell-tale signatures in the force or position data. The last category is Multiple Bond Models, and is those methods which attempt to extract single molecule characteristics from data which is known to contain multiple molecules. After the discussion of these methods, we define two simple criteria for ensuring specific single molecule measurements, and use these criteria to examine the literature on the strength of the biotin-streptavidin bond. We find that those publications that meet the criteria have very similar results for the strength of the bond, providing evidence that some of the inconsistency in studies of the biotin-streptavidin bond is due to data contamination by multiple bonds. While this review focuses on molecular bonds, most of the methods described can also be applied to other SMFS applications such as protein unfolding.

General SMFS

There are several different instruments for measuring the force dependence of bond lifetimes including the atomic force microscope (AFM), optical trap (OT), magnetic tweezer (MT), and biomembrane force probe (BMFP). The first three of these instruments are well reviewed in Neumann and Nagy [15] and a description of the BMFP can be found in Gourier et al., [16]. While these instruments have many differences in form and operation, the procedure for gathering single molecule measurements is similar.

In general, a probe is coated in a biomolecule, and a separate surface is coated with a complimentary biomolecule. The methods for attaching the biomolecules to the probe/surface are numerous and will depend on several factors including the biomolecules being used and the material composition of the probe/surface. The probe is then brought into close proximity with the surface until one or more bonds form (Figure 5A). For the AFM, OT, and BMFP, the probe or surface is then retracted at a constant velocity until the bond ruptures, which is detected via an instantaneous displacement of the probe (Figure 5B). This method of retracting the probe at a constant velocity is known as Dynamic Force Spectroscopy (DFS). The MT uses a magnetic field to apply a constant force to magnetic beads (probes), and therefore the velocity of the beads is variable, but the force on the beads is constant. This method is known as Constant Force Spectroscopy (CFS).

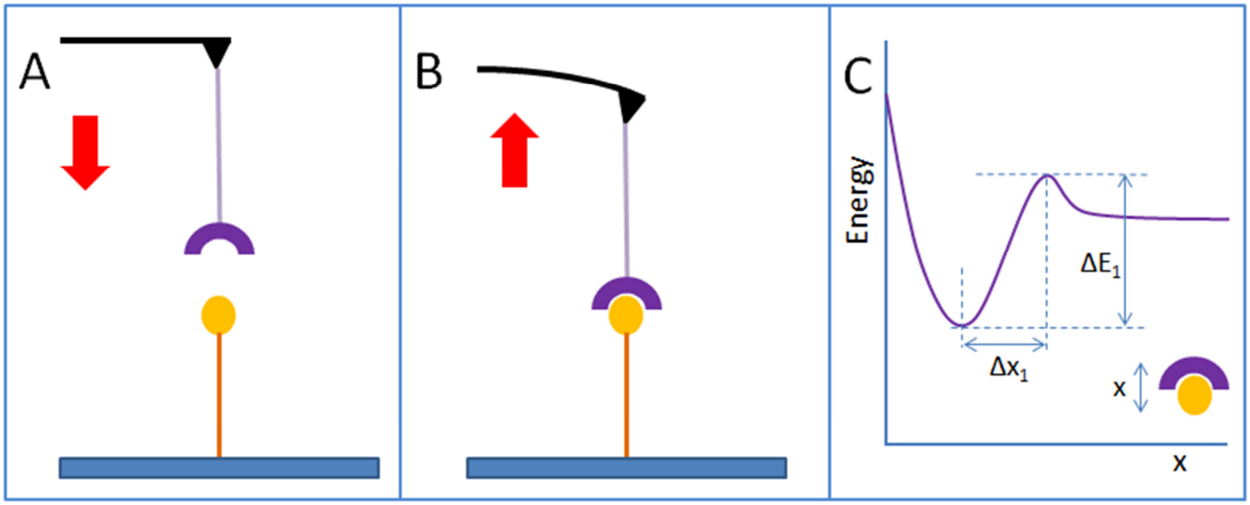

Figure 5: A.) A conceptual illustration of an AFM cantilever approaching a surface allowing two biomolecules to interact. B.) After bond formation, the cantilever is retracted at constant velocity until bond rupture. The force on the cantilever is estimated by the cantilever deflection. C.) An illustration of the energy landscape of a simple bond.

A simple energy model for a bond is shown in Figure 5C. The landscape has two low energy conformations separated by a single barrier, whose peak is separated from the low energy state by Δx_1, and has height ΔE_1, where the subscripts represent the pathway to unbinding. The transition rate from state one, k_1^0, is proportional to $\exp\left(\frac{\Delta E_1}{k_B T}\right)$, where $k_B T$ is thermal energy. Bells model predicts that as a force f is applied to the bond, the energy barrier will decrease by $f \times \Delta x_1$ [13]. Force thus affects the transition rate exponentially as shown in Equation 1.

$$k_1(f) = k_1^0 * \exp\left(\frac{f * \Delta x_1}{k_b T}\right) \qquad \text{Equation 1}$$

For more complex energy landscapes which may have multiple energy barriers and escape paths, Equation 1 becomes

$$k_i(f) = k_i^0 \times \exp(\frac{f \times \Delta x_i}{k_b T}), \qquad \text{Equation 2}$$

and the total transition rate for all the pathways is the sum of the transition rates for the n possible escape paths,

$$k(f) = \sum_{i=1}^{n} k_i\,(f). \qquad \text{Equation 3}$$

By estimating the rate constants k_i^0, and distance constants Δx_i in equation 2, the expected rupture force or bond lifetime can be determined under various experimental conditions. Thus, when testing the effect of a mutation, construct truncation, or antibody on the bond, there will be a baseline from which to gauge any difference in bond function.

The methods to determine the constants k_i^0 and Δx_i, are different for DFS and CFS studies. Using DFS, the standard approach is to examine the force at which each bond ruptures using different loading rates r which is a product of the probe velocity and the spring constant of the probe. Due to the stochastic nature of bond rupture, there will be a distribution of rupture forces for any single loading rate, as shown in Figure 6A. The peak of this distribution corresponds to the mean rupture force F^*. By determining the mean rupture force for several different loading rates, the rate and distance constants can be estimated using equation 4 [29].

$$F^* = \frac{k_b T}{\Delta x_1} \ln \frac{r \Delta x_1}{k^0 k_b T} \qquad \text{Equation 4}$$

For CFS experiments, the fraction of surviving bonds as a function of time are examined and are known as survival plots (Figure 6B). The force-dependent off rates $k_i(f)$ and average bond lifetime can be determined directly from this plot by calculating the slope of the data, which will be linear for single-state bonds when the ordinate is viewed on a logarithmic scale. By calculating $k_i(f)$ for multiple forces, the off-rate constants k_i^0 and Δx_i can be estimated using equation 2 [14].

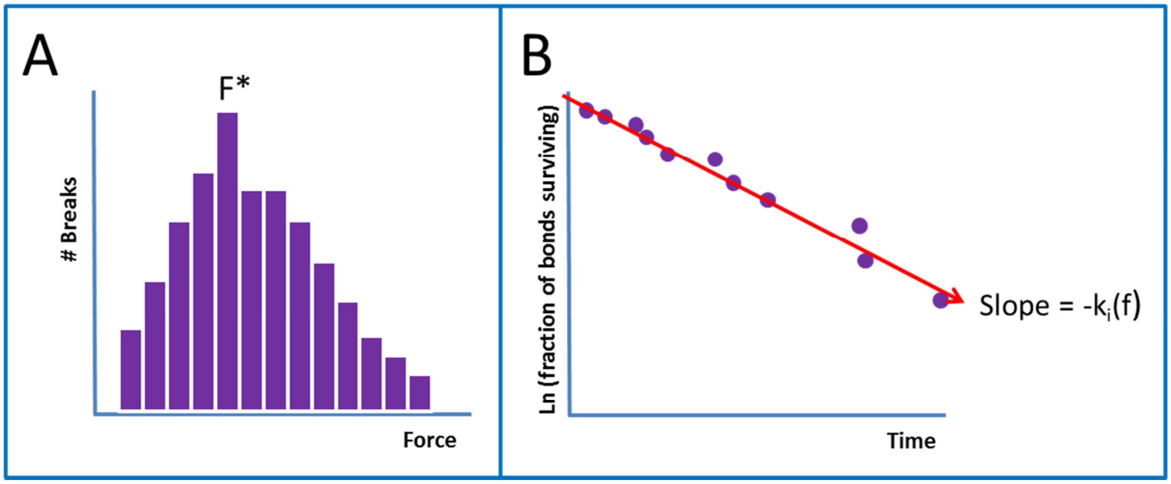

Figure 6: A) Illustration of a histogram of rupture forces for a single loading rate r using DFS. Determination of the mean rupture force F^* for several load rates yields estimates for k_i^0 and Δx_i using Equation 4. B) Illustration of the fraction of bonds surviving as a function of time for a CFS experiment. When viewed on a logarithmic scale, the slope of the data can be used to determine $k_i(f)$. Survival plots for different forces allow estimates of k_i^0 and Δx_i using Equation 2.

The models described above for modeling kinetic bond behavior apply only to specific interactions of single bonds. Non-specific interactions can be troublesome to overcome but are outside the scope of this paper. For more information on the sources of nonspecific interactions, please see Vanoss [30].

Reducing Multiple Bonds

The process of a probe approaching the surface such that bonds can form, and then applying a constant loading rate or force until bond rupture is known as a force cycle, and is the combination of Figure 5A and Figure 5B. As will be discussed in proceeding sections, it is not a trivial matter to differentiate force cycles which have formed one bond with those that have formed multiple bonds. However, there are methods that reduce the probability of forming multiple bonds. This can be done either by reducing the adhesion rate, or by functionalizing surfaces such that only a single bond can form. These methods are described below.

Low Adhesion Rate

If the binding during the force cycle can be considered a stationary-random process, and bonds form independently i.e., no dimerization or aggregation, then the probability of bond formation follows a Poisson distribution [18]. If the adhesion rate, or probability of a force cycle forming one or more bonds, is considered A_w, then the probability of zero bonds forming is

$$P_0 = (1 - A_w). \qquad \text{Equation 5}$$

The Poisson distribution predicts that the probability of forming exactly one bond is

$$P_1 = (A_w - 1)\ln(1 - A_w)\ , \qquad \text{Equation 6}$$

and the probability of forming more than one bond is

$$P_{n\geq 2} = A_w + (1 - A_w)\ln(1 - A_w)\ . \qquad \text{Equation 7}$$

Thus, if there is a 50% chance of bond formation ($A_w = 0.5$) then 31% of bonds will be multiple bonds. However, if A_w is reduced to 0.1 then less than 5% of bonds will be multiple bonds.

Decreasing A_w can often be achieved by decreasing the concentration of biomolecules on either the probe or surface, decreasing the contact time of the probe with the surface, or by decreasing the contact area between the probe and the surface. Recent research in this area has shown that the small surface area between an AFM probe and highly curved carbon nanotubes often results in single bonds [31].

For cases of multiple single-state bonds in series or parallel configurations, analytical descriptions have been developed that predict the off-rate as a function of the number of simultaneous bonds [28]. In the case of multiple bonds in series each bond experiences the entirety of the force on the probe, and the off-rate for N bonds becomes

$$k(f,N)_S = \left[\sum_{i=1}^{N}\left(\frac{1}{k^0}\exp\left(-\frac{fx}{k_bT}\right)\right)\right]^{-1}. \qquad \text{Equation 8}$$

In the case of parallel loading, the force on the probe is shared by the bonds, and the off-rate is

$$k(f,N)_P = \left[\sum_{i=1}^{N}\left(\frac{1}{nk^0}\exp\left(-\frac{fx}{nk_bT}\right)\right)\right]^{-1}. \qquad \text{Equation 9}$$

The use of Equation 7 allows an estimation of the amount of multiple bond measurements to expect from the adhesion rate, while equations 8 and 9 determine the expected off-rate for these measurements. Thus, for cases of mostly single bond data, if a fraction of outlying data is similar to the amount expected from Equation 7, and this data shows off-rates similar to the predictions from equations 8 or 9, then this provides evidence that the outlying data may be due to multiple bonds. However, care should be taken when using this method, since complex bonds with multiple states or pathways have demonstrated behavior similar to a simple bond with a mix of single and multiple bonds [9, 32].

Poisson statistics shows that using a low adhesion rate reduces the proportion of multiple bond measurements. However, using a low adhesion rate means that the vast majority of force cycles will not form bonds, adding substantial experimental time to achieve significant results. Additionally, reducing the rate of specific adhesion while the rate of non-specific adhesion remains constant is undesirable and essentially reduces the signal to noise ratio of the experiment. In general, we recommend reducing the adhesion rate to less than 20%, such that the probability of forming multiple attachments is less than 2%. However, higher adhesion rates may be justified if the experimenter uses one of the other proven methods described below. For example, if a single bond signature is used, then multiple bond interactions can be identified and removed from the data. In this case, it would be advantageous to use the adhesion rate that yields the largest rate of single bonds, when A_w ~ 0.63.

Single Molecule Interactions

Traditional techniques of functionalizing surfaces results in randomly spaced biomolecules. Therefore, even at very low biomolecule concentrations there is a possibility of multiple bonds forming, the probability of which can be estimated using Poisson statistics. An alternative process is functionalizing surfaces using regularly spaced arrays where the spacing between biomolecules is controlled. If the spacing of biomolecules in a regular array is increased such that a probe can only interact with a single biomolecule at a time, then there is no way for multiple bonds to form. Using microcontact printing of DNA end binding labels, regular arrays have already been used to increase the multiplexing ability of a magnetic tweezers assay [21].

A similar approach involves functionalizing probes with a single biomolecule. Recent research in this area has demonstrated AFM cantilevers functionalized with just a few biomolecules [33, 34], with the number of biomolecules quantified using quantum dots [33, 35]. If these methods can be improved so that cantilevers can be functionalized with a single biomolecule, then there would be no mechanism for multiple bonds to form between the probe and the surface.

Functionalizing surfaces such that only single bonds can form negates the need for low adhesion rates, and would therefore increase the throughput of experiments. However, there are significant technical challenges remaining for both of the methods described. In order to eliminate the possibility of forming multiple bonds with regular arrays, each location in the array would need to be a single biomolecule, which has not been demonstrated with current micro-etched arrays. Similarly, reducing the number of biomolecules on a probe can reduce the probability of multiple bonds forming, but until a probe can be functionalized with a single biomolecule there is no guarantee that measurements are of single bonds. This ability to reliably functionalize a probe with single biomolecules has not yet been demonstrated.

Single Bond Signatures

Single bond signature methods can be used to differentiate single bond data from multiple bond data via position or force signatures that can only be due to single bonds. Using these methods, the experimenter can disregard multiple bond data. Single bond signature methods are an alternative to the use of a low adhesion rate, and have the benefit of not requiring a low adhesion rate, thereby decreasing the experimental time needed to achieve statistically significant results.

Probe Oscillation

The BMFP, OT, and MT all have probes that are free to oscillate in three dimensions, and all three instruments track the position of the probe in three dimensions. This ability to track the probe multidimensionally can be used to determine if one of more bonds are attached to the probe [24]. Consider a small magnetic bead that is used as a probe in a MT study. Before the bead attaches to the surface, thermal fluctuations will cause the bead to oscillate in a random pattern in three dimensions. However, once the bead forms an attachment to the surface, the variation in position will be reduced (Figure 7A). If the bond tether lacks a preferred orientation, then a histogram of the bead position in the x-y plane will show a circular pattern around the tether attachment point (Figure 7B). However, if two bonds form, then the movement of the bead along the axis between the two attachment points will be restricted, and result in a histogram with an elliptical pattern (Figure 7C). Creating accurate histograms of position data requires acquiring large amounts of position data, which can make this method less applicable for short-lived bonds.

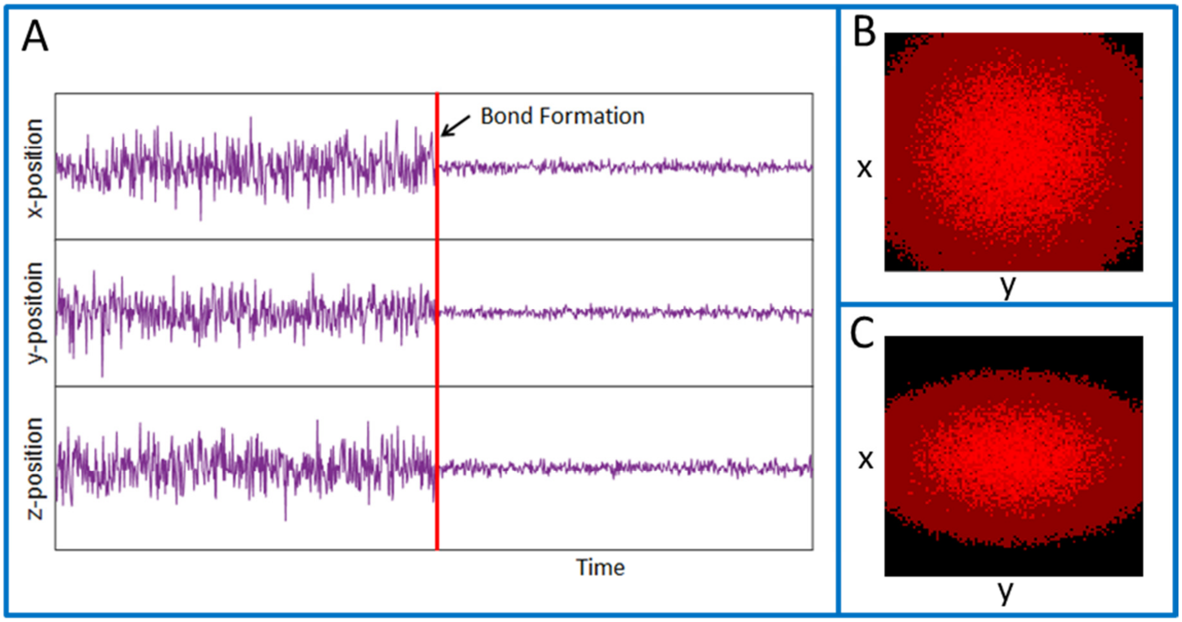

Figure 7: A) Simulated position data demonstrating a reduction in position noise once a bond forms. B) Simulated histogram data for a bead with a single bond, which shows a circular pattern

around the attachment point. C) Simulated histogram data for a bead with two bonds. Restriction in movement along the axis between the attachment points results in an elliptical pattern.

Mechanical Fingerprints

In this context, a mechanical fingerprint is an indication in the force-position data that can differentiate between single and multiple bonds. This usually involves coupling flexible linkers or biomolecules with known force signatures (marker molecules) to the bond of interest [36-39]. A worm-like-chain (WLC) or freely-jointed-chain (FJC) model can then be fit to the force-position data [38] and used to identify multiple bonds by examining the extension of the linker [40, 41], or the contour length of the marker molecule [38]. WLC and FJC models can also be used to more precisely determine bond barrier locations [42]. An additional advantage of using flexible linkers or marker proteins is that the bond rupture occurs far from the surface, which reduces non-specific interactions [41, 43, 44]. Three different configurations for using mechanical fingerprint are discussed below.

In the first configuration, a marker molecule is coupled to the bond of interest [45-48] (Figure 8A). Marker molecules typically have an unfolding event that occurs at a known force. This unfolding force can therefore be used as a test for multiple bonds, assuming the unfolding force is smaller than the bond rupture force. Alternatively, if the bond is coupled with multiple marker molecules in series, there will be a series of unfolding events. In this case, multiple contour lengths can be examined to determine if there are multiple bonds [38]. Marker molecules with known force signatures include titin [49], fimbriae from *E. coli* [50-52], ubiquitin [53], single filamin A [54], and DNA [5]. A review of the use of marker molecules and polyproteins in SMFS can be found in Hughes and Dougan [38].

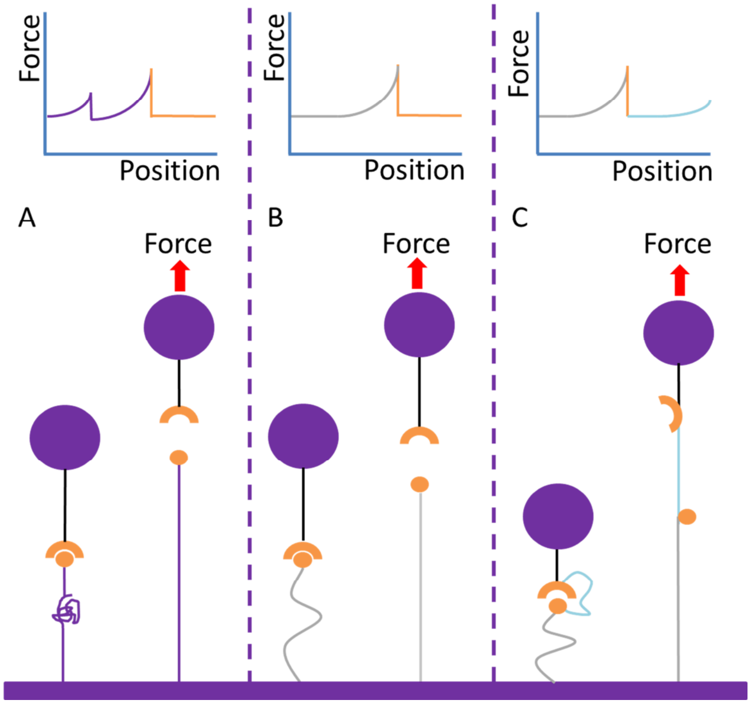

Figure 8: Mechanical fingerprint configurations. A.) A marker protein with a known force signature (purple) is linked to a bond-forming protein (orange). B.) Using a long, flexible linker such as PEG (gray) is the simplest configuration. C.) A looped linker using a molecular tether (cyan) allows repeated testing of the bond kinetics.

The configuration in Figure 8B uses long flexible linkers such as polyethylene glycol (PEG). The extension of the PEG linker under force can be used to determine if there are multiple bonds [40]. PEG has the advantage of being commercially available with a number of different functionalization options, and does not require any significant protein engineering. Besides PEG, a variety of other linkers have been demonstrated including m13 bacteriophage[55], DNA [56] and polymeric handles with multiple binding locations [57, 58].

A more recent configuration for examining bond kinetics is a looped linker [41, 59-61] where the biomolecules of interest are attached via a molecular tether (Figure 8C). This provides the unique opportunity of repeatedly testing the same biomolecular pair, which can increase experimental throughput, and allows the study of heterogeneity in the bond population [60]. If the bond complex is attached to the surface via a long flexible linker, then the extension of the linker can be used as a mechanical fingerprint. Alternatively, a coupled marker molecule can be used to unambiguously identify multiple bonds [41].

Using mechanical fingerprints is not always applicable, and can increase the complexity of the experiment and data analysis. For example, when adding marker molecules to the construct of a bond, the linkers or proteins must unfold at forces below the rupture force of the bond. Unfortunately, the unfolding force of many commonly used marker molecules is higher than that of most bonds [38]. Also, the use of long, flexible linkers can lead to errors in kinetic parameter estimates and requires corrections to be accurate [62-64]. Lastly, some linkers, especially looped linkers, can be difficult to create without expertise in protein engineering and purification [41].

Single Rupture Force Cycles

Figure 9 shows an example force cycle with multiple bonds where each jump in force represents one or more bond ruptures. Some studies have sorted this force data by considering only force cycles that show a single rupture event [29, 65], or only using the last rupture event in the force cycle [23, 25].

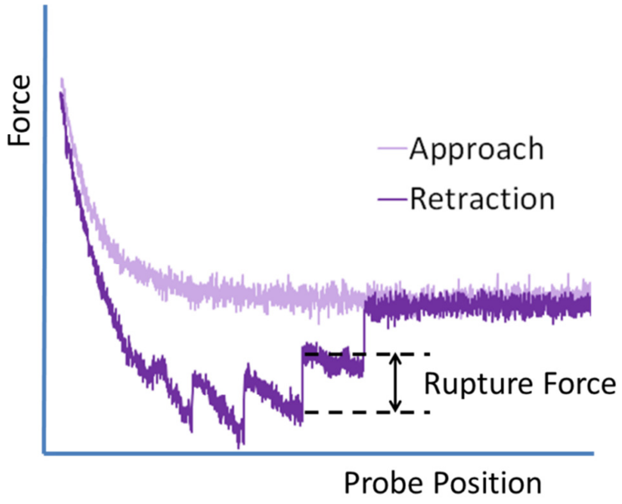

Figure 9: A typical force-displacement curve for an AFM. Each instantaneous change in force represents one or more bond ruptures.

An assumption for both of these techniques is that rupture events occur significantly far apart in time and space so as to be detectable, i.e. what looks like a single rupture is not multiple simultaneous ruptures. However, as the adhesion rate increases, so does the probability that two ruptures occur close enough together to be undiscernible, known as a false single bond. Simulations examining this phenomenon were performed by Getfert and Reimann [66] and found that under certain conditions when the adhesion rate is 70%, the probability of observing a false single bond is greater than 20%, and remains above 10% when the adhesion rate is just 50%. Another study that examined the prevalence of false single bonds used a histogram of the distance between rupture events (Figure 10). By extrapolating a model of the data to distances smaller than the spatial resolution of the instrument, the fraction of false single bonds was estimated [67]. These two studies demonstrate that without a low adhesion rate, force data that looks like single bonds may actually be contaminated with undetectable multiple bonds.

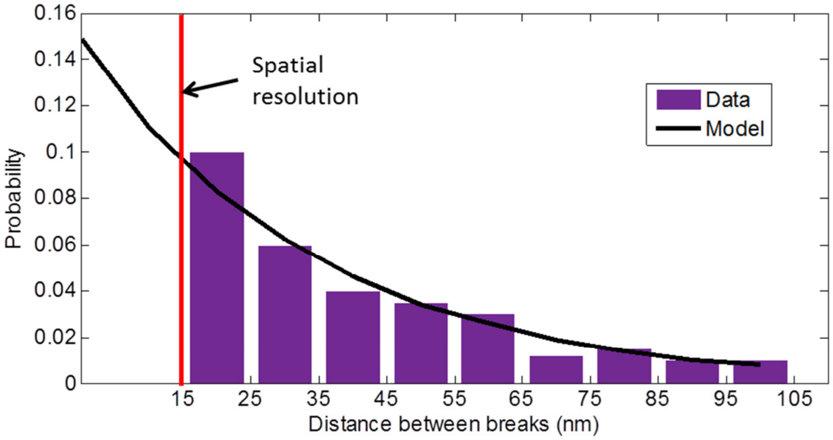

Figure 10: Illustration of histogram data of distance between bond breaks for an instrument with 15 nm of resolution. The model is an exponential fit to the histogram data. By extrapolating the model to distances below the spatial resolution of the instrument, an estimation for the probability of false single bonds can be made [67].

Multiple Bond Models

Using the methods described in Reducing Multiple Bonds and Single Bond Signatures can make experiments more technically challenging and can increase the time it takes to collect data. Thus, there have been many efforts to develop models to extract single bond properties from multiple bond data. One such approach that uses an autocorrelation of force histograms [25, 68], has been shown to provide inaccurate results [28]. Another model which uses assumptions from a Poisson distribution [27, 69, 70], has been found to be inaccurate unless very low adhesion rates are used [28].

To evaluate the reliability of the remaining models [71-74] we considered whether the models demonstrated an ability to determine accurate single bond kinetics from multiple bond data. Accuracy was determined by comparison to a study where data was demonstrably primarily single bonds. This single bond data had to have a negative control, and also use either a low adhesion rate (< 35%) or one of the reliable Single Molecule Signature methods. As is demonstrated in the discussion of the biotin-streptavidin bond, we find that these two criteria are effective in ensuring that the majority of data is due to single bond measurements. Of the remaining four models, only the model by Huang *et al*., [74] met the criteria. This model predicts that homodimers form longer lived bonds through a ligand rebinding and exchange mechanism. This model was confirmed experimentally by comparing monomeric and dimeric cRGD (cyclic Arg-Gly-Asp) unbinding from integrin (αvβ3) with an atomic force microscope.

Single Bond Methods Summary

Single molecule force spectroscopy elucidates the function and mechanism of biological interactions that were previously unexaminable. However, in order for this power to be realized there must be a diligent and rigorous standard of methodology to ensure trustworthy results. We have discussed the different methods used to confirm that measurements are due to single bonds, with each method having advantages and drawbacks, summarized in Table 1.

Method	**Objective**	**Reliable?**	**Drawbacks**
Low Adhesion Rate	Estimate proportion of multiple bonds	Yes	Decreased data acquisition rate
Single Molecule Interactions	Ensure single bond measurements	Has not been demonstrated	Complex surface functionalization

Probe Oscillation	Identify single bond measurements	Yes	Requires large amounts of position data
Mechanical Fingerprints	Identify single bond measurements	Yes	Complex data analysis, significant protein engineering
Single Rupture Force Cycles	Identify single bond measurements	No	Unreliable due to hidden multiple bonds.
Multiple Bond Models	Extract single bond kinetic parameters from multiple bond data	Uncertain. Only one model [74], met reliability criteria.	Most models are unproven

Table 1: Summary of methods used to examine single bonds.

Based on this analysis, we suggest two simple criterions for assessing whether a study has adequately demonstrated single bond behavior. The first criterion is that one of the reliable methods shown in Table 1 is thoroughly demonstrated. If using a the Low Adhesion Rate method, we recommend an adhesion rate of < 35%, such that a Poisson distribution predicts 80% of bonds to be single bonds. The second criterion is that there must be a negative control experiment in order to demonstrate specificity of the measured adhesion. Negative controls usually entail, in the case of a receptor-ligand bond, adding either excess receptor or ligand to the system, or by not having either the receptor or ligand present. While the negative control may seem a trivial step, it is also paramount to ensuring that the adhesion is due to the binding of the biomolecules of interest.

The Biotin-Streptavidin Bond

The biotin-streptavidin bond has been widely studied using dynamic force spectroscopy since 1994 when measurements of its rupture force were studied via AFM [75]. However, there has been disagreement about the strength of the bond, and its kinetic parameters. For example, three publications [26, 76, 77] found rupture forces between 130 pN and 180 pN at ~1000 pN/s loading rate, while others report rupture forces between 45-80 pN [1, 29, 78]. The hypotheses behind this discrepancy include differing spring constants [65], multiple bond formations [23], the age of the bond [79], and temperature [78].

As a biomolecular complex that is widely used and discussed, it's troubling that so many different results come from similar measurement techniques. If there cannot be adequate agreement on a receptor-ligand system that is relatively well known then how can results on other biological bonds, which will be less understood, be trusted? It seems that there must be an accepted standardization on how to go about these studies, and how the results should be interpreted. Here, we applied the two criterions suggested in the summary of the methods, and demonstrate that when these criteria are applied to the literature, those publications meeting the criteria are in relative agreement as to the bond strength and kinetic parameters of the biotin-streptavidin bond.

Certain publications [68, 75, 76] on the biotin-streptavidin bonds have very high adhesion rate (> 50%) and did not use either the Probe Oscillation or Mechanical Fingerprint methods. One of these publications attempted to isolate single bond ruptures based on using only the last rupture in the force curves. However, as described earlier in the section on Single Force Cycles, at high adhesion rates there can be a significant number of multiple bond ruptures that can be mistaken as single bond ruptures [66]. There was also an attempt to use autocorrelation on probability density functions to determine single bond rupture force. Again, this was shown to be an incorrect technique for interpreting data [28] as bond rupture force is not proportional to the number of bonds attached. Because these publications did not meet the first criteria, they were rejected from further analysis.

Several publications did not use any of the reliable methods described in Table 1 [23, 29, 77, 80-83] while others did not demonstrate the specificity of their measured adhesion with a negative control [65, 72, 79, 84-86]. It was therefore difficult to evaluate the prevalence of multiple bonds or specificity of the attachments formed. These publications were thus considered unreliable and were also excluded from the analysis.

Lastly, there were two publications that met both criteria above, yet were discarded. The first, Lo *et al.*, has a system with such a high noise threshold ~30 pN , that it would have been difficult to impossible to differentiate bond breaks from noise, assuming that bond breaks occur at ~30 pN, which has been shown [27] . This publication also utilized a method that uses assumptions associated with a Poisson distribution to estimate rupture force. This method is described in the Multiple Bond Analysis section and was shown to be inaccurate except at very low (<5%) adhesion rates [70]. However, Lo *et al* used a 33% adhesion rate and it therefore seems that the mean rupture forces found in this paper are questionable.

The second publication, Yuan *et al.*, claimed an adhesion rate of 25%, yet shows figures of force cycles that had several rupture events, which seems unlikely if their the adhesion rate was truly 25% [26]. More problematic is that rupture events below ~75 pN were not included in their probability density functions, even though their example force cycle showed two events of ~50 pN. It thus seems that the data analysis was biased towards higher rupture forces, which may have been hidden multiple bonds.

Author,Year	**Rutpure force (pN) @ 1000 pN/s**	**Inner barrier location (nm)**	**Outer barrier location (nm)**
Merkel *et al*. [1]	75	0.12	0.5
Rico and Moy [78]	65	0.09	0.38
Guo *et al*. [71]	45	0.28	0.46
Taninaka *et al*. [87]	50	0.13	0.63

Table 2: Publications that met criteria for single bond measurements and the corresponding results for rupture force at a 1000 pN/s loading rate, and the inner and outer barrier locations.

Table 2 shows the four publications that met the two criteria, and their results for the rupture force and barrier locations. All of the publications in Table 2 show low rupture forces as opposed to the 120-150 pN found in other publications. Also, the barrier locations are very similar, except for perhaps the inner barrier found by Guo et al. This may be due to the “two-bond” model for interpreting data that was being demonstrated [71]. One possible reason for the differing rupture forces in Table 2 may be the effective spring constants of the system. For example, Walton et al., showed that the effective spring constant can have a significant effect on rupture force, even when the same loading rate is used [65]. Another possibility is the temperature at which the experiments were conducted: Rico and Moy demonstrated that a temperature difference of 17 °C can change the rupture force by two-fold [78].

Our analysis above suggests that some of the discrepancy seen with the biotin-streptavidin bond is due to improper experimental methods to reduce multiple bond formations. By implementing relatively simple criteria based on sound theory and experimental support, we were able to narrow the published works to those that demonstrated strong evidence of single bond measurements. Those publications that met the criteria had results that were in agreement. We hope that understanding the techniques described above will help fellow researchers design more accurate and efficient SMFS experiments, and also aid readers in critically evaluating publications in this field.

Chapter 2: The MMTB

Abstract

Our custom built magnetic tweezer combines high multiplexing, precision bead tracking, and bi-directional force control into a flexible and stabile platform for examining single molecule behavior. Here we describe the instrument and its ability to apply 2-260 pN of force on up to 120 beads simultaneously, with a maximum spatial precision of 10 nm using a variety of bead sizes and experimental techniques. We also demonstrate a novel method for increasing the precision of force estimations on heterogeneous paramagnetic beads using a combination of density separation and bi-directional force correlation which reduces the coefficient of variation of force from 27% to 6%. We then use the instrument to examine the force dependence of uncoiling and recoiling velocity of type 1 fimbriae from *Eschericia coli* (*E. coli*) bacteria, and see similar results to previous studies.

Introduction

Single molecule force spectroscopy (SMFS) has become a powerful tool for investigating the force dependence of biological phenomenon [15]. SMFS techniques have been used in a variety of applications including, but not limited to, the determination of biological bond lifetimes [1-3], viscoelastic cell properties [4], DNA stretching [5], and the characterization of motor proteins [6, 7]. However, the traditional SMFS methods of atomic force microscopy, optical trap, and biomembrane force probe can only examine a single molecule at a time. Since some studies require hundreds to thousands of measurements to accurately model force dependence, such as the stochastic process of biological binding [12], gathering statistically sufficient data via traditional SMFS methods can take a prohibitively long time.

The magnetic tweezer (MT) is a relatively recently developed instrument that allows the examination of hundreds of single molecule measurements simultaneously [21, 88, 89], significantly reducing data acquisition time. In a generic MT assay the biomolecular complex has one end attached to a surface and the other end to a paramagnetic bead suspended in a chamber (Figure 11A). The chamber typically is two glass slides separated by double sided tape containing a solution of the beads in buffer. A magnetic field gradient, generated by magnets above the chamber, pulls the beads away from the surface at constant force. The beads are viewed via a high-speed camera through the objective of an inverted microscope. By examining the position of the beads over time, the force dependent properties of the biomolecular complex can be determined. Many beads can be fit in the field of view, leading to the MT's multiplexing capability. However, to fully take advantage of multiplexing requires the simultaneous implementation of other capabilities that have only been demonstrated separately.

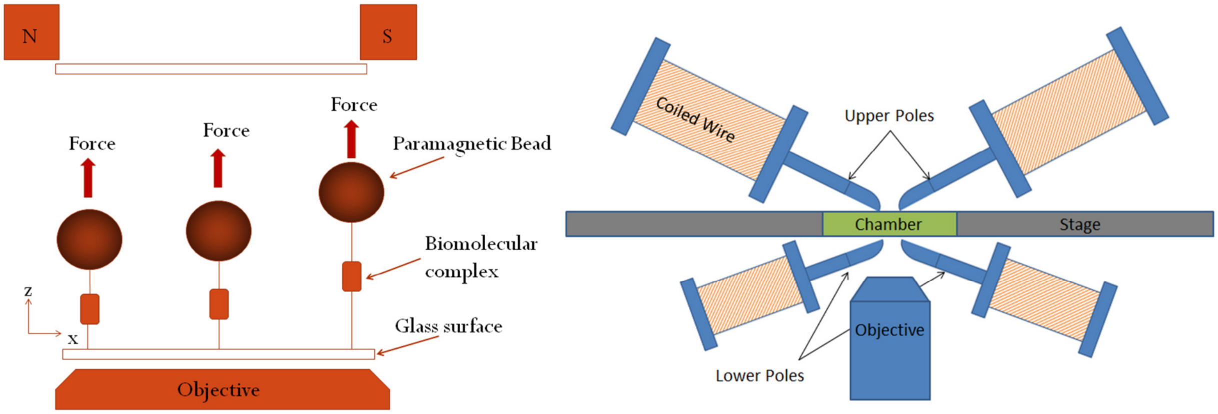

Figure 11: A.) An illustration of a generic MT assay. B.) An illustration of the MMTB.

The smallest detectable change in the height of a bead is referred to as the spatial resolution and determines the lower limit of biological length changes that can be detected. The spatial resolution in basic MT's is estimated using the depth of field and is on the order of several microns [90]. However, by implementing high precision particle tracking algorithms, the spatial resolution can be improved to less than a nanometer [22, 91, 92], greatly expanding the biological questions that can be addressed [21, 89, 93-99]. The use of magnets both below and above the chamber allows beads to be pulled toward and away from the bottom surface [90]. This bi-directional force control allows greater control of the contact time of the beads with the surface: an important parameter for performing reproducible experiments. To our knowledge, a magnetic tweezer combining the three capabilities of multiplexing, precision bead tracking, and bidirectional force control has not been demonstrated.

Here we describe a multiplexed magnetic tweezer with precision bead tracking and bi-directional force control (MMTB) and characterize its capabilities. Because high forces of up to 100 pN are desired for many studies and pose unique challenges for multiplexing with electromagnets, we describe use of the MMTB to obtain this force range. To achieve these high forces, large paramagnetic beads with high magnetic content were used. These beads showed significant bead to bead force variation, which can prohibit the accurate estimation of force dependent properties. To address this challenge, we developed a novel method for precisely determining forces on beads with heterogeneous magnetic content, which reduced the coefficient of variation of force from 27% to 6%. We further demonstrate that there are tradeoffs between optimizing multiplexing, tracking resolution, and applied force. We then used the MMTB to examine the uncoiling and recoiling velocities of *E. coli* fimbriae under a wide range of forces.

Description and Characterization of the MMTB

Hardware

The MMTB uses four electromagnetic poles: two above and two below a chamber containing paramagnetic beads suspended in buffer (Figure 11B). The design and orientation of these magnets is similar to those described by Snook and Guilford [90]. Each electromagnetic pole consists of a 6.6 mm diameter Mu-metal rod (GoodFellow, Coraopolis, PA) with the tip shaped to maximize the gradient of the magnetic field [100]. The Mu-metal rods are encased in spools with several hundred turns of 26 AWG copper wire wound around them. The upper poles are placed very near to the top surface of the chamber, with a separation distance between the poles of ~ 1 mm. The lower poles, due to spatial constraints below the flow chamber, are spaced ~ 7 mm apart and ~3 mm below the chamber. This reduces the magnetic field that pulls beads down, but this suffices.

By applying a voltage potential across the coils using two identical power supplies (1697, BK Precision, Yorba Linda, CA), a magnetic field gradient acts to pull the beads in the upward (upper magnet) or downward (lower magnet) direction. In practice, the lower magnet is first used to pull the beads to the bottom surface, the current to the lower magnet is then turned off and the current to the upper magnet turned on, and the beads are pulled away from the surface at a force controlled by the magnetic field. This cycle of pulling the beads toward and away from the surface is known as a “pull”. A high speed camera (GT1910, Allied Vision, Exton, PA) is mounted to an inverted microscope (Eclipse TI-E, Nikon, Melville, NY) and used to acquire images of the beads at rates of up to 100 Hz, using either a 0.45 NA 20x or 0.55 NA 40x objective. The use of objectives with longer working distances and low NA’s is due to spatial constraints below the chamber caused by the lower magnet. With the 20x objective, 40 7.8 µm diameter beads or 120 2.8 µm diameter beads can fit in the field of view (528 x 297 µm), with enough space between beads to allow tracking, i.e. diffraction patterns do not overlap.

A custom Labview program (National Instruments Corporation, Austin, TX) is used to provide synchronous control of the microscope, power supplies, and camera. The Labview program allows the camera and power supply settings to be adjusted in real time, or a time-based script can be used to ensure repeatability between pulls. This flexibility is beneficial when measuring bond lifetimes: one may need a high frame rate to see very short lived bonds, and then switch to a lower frame rate to see the longer lived bonds, thus avoiding collecting superfluous amounts of data. Using the Labview program, we found that it takes ~40 ms to switch from one current level to another (data not shown), similar to the findings by Snook and Guilford [90].

Bead Tracking

Experimental images are analyzed using a custom Matlab script (MathWorks, Natick, MA) similar to other particle tracking algorithms [22, 91]. In short, as the spherical paramagnetic beads travel in the z-direction (along the axis of the objective), the diffraction pattern of the beads change as they move in or out of focus. Before each experiment a lookup table is created which determines a vector of the pixel intensities in the radial direction, or radial intensity vector, of a representative bead at different z-positions by moving the objective small axial steps while the beads are stationary. During the experimental pulls, when the beads are moving and the objective is stationary, the radial intensity vectors of all the beads in the field of view are extracted and compared to the lookup table to estimate their z-positions. By comparing the bead position using lookup tables from several different beads, the accuracy of the position estimation can be further improved.

To estimate the tracking accuracy of the MMTB over long distances, we tracked several beads under force as the beads traversed the axial distance of the chamber (~78 µm). We then compared this to the chamber height, as measured by focusing on beads that were stuck to the top and bottom of the chamber and noting the microscope objective position. The measured height was within a few percent of the chamber height with an error of 2.9 ± 0.5% (SEM) for 7.8 µm beads. This demonstrates that our system is capable of accurately tracking beads over long distances, an important ability when estimating the force on beads (described in Force Calibration).

To test the spatial resolution, we non-specifically bound beads to the surface, and determined their z-positions over time. The resolution is computed as the standard deviation of the bead displacement. We determined this resolution at 40x magnification under various conditions for the 2.8 µm diameter beads (Figure 12A). Examining raw data, the resolution is about 75 nm, which may primarily reflect stage vibration. By subtracting the position of another bead in the field of view, known as a reference bead, any movement of the stage is accounted for and the resolution is improved to 30 nm. Subtracting the average position of five reference beads shows only a small improvement over the single reference bead. The combination of five reference beads and a five-point rolling time average results in a resolution of 10 nm. However, this rolling time average sacrifices temporal resolution, and therefore may not be suited for studies on small time scales. This data shows the large effect of stage vibration on spatial resolution, and that precision cannot be optimized without sacrificing temporal resolution.

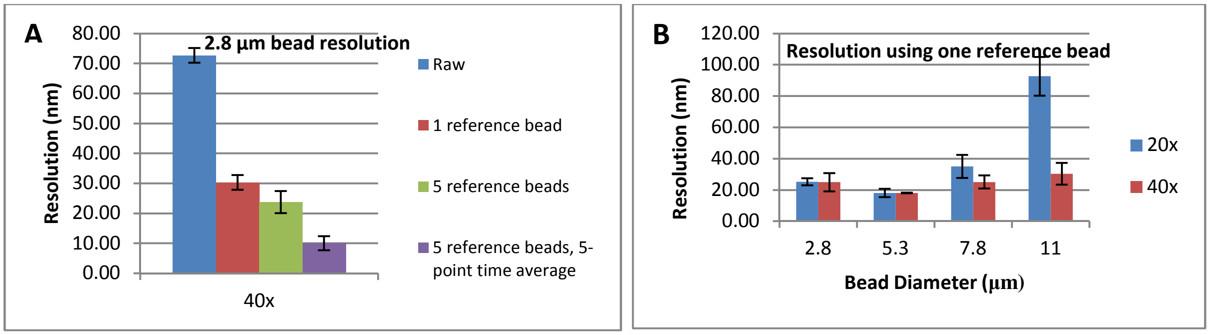

Figure 12: A.) Resolution of 2.8 µm beads for different conditions using a 0.55 NA 40x objective. B.) Resolution using different sized beads when subtracting one reference bead using a 0.45 NA 20x objective and a 0.55 NA 40x objective. All error bars represent the standard error of the mean (SEM) of two separate data sets of 3-9 beads obtained on different days.

To examine the effect of objective properties and bead size on spatial resolution we determined the spatial resolution for beads of different sizes using a 0.45 NA 20x and 0.55 NA 40x objectives while using a single reference bead (Figure 12B). At 20x, the resolution is quite similar for the 2.8-7.8 µm beads but increases dramatically for the 11 µm beads. At 40x, the resolution is a relatively constant 18-30 nm for all bead sizes. Considering that the twofold higher magnification objective results in a four-fold reduced field of view and throughput, the small improvement in resolution may be unwarranted for most experiments. Also, since the resolution of beads ranging from 2.8-7.8 µm is similar, the choice of bead size should be based on the desired force range and level of multiplexing: larger beads can achieve higher forces, but fewer can be tracked simultaneously.

Force Calibration

The force on the beads can be estimated from the velocities by determining the z-position of the beads as a function of time and then applying Stokes' Law,

$F = 6\pi\mu r v\lambda,$ Equation 10

where F is the drag force on the bead, μ is the dynamic viscosity of the fluid, r is the radius of the bead, v is the velocity of the bead, and λ is the correction factor due to the chamber wall effects. λ is dependent on the chamber height, position of the bead relative to the walls, and the size of the bead. Approximations for λ have been determined previously and can be estimated for a variety of conditions [101, 102]. When using 7.8 µm beads, λ was estimated to be 1.2 for our experiments. For a detailed explanation of the approximations for λ in this publication, please see Supplementary Materials.

We determined the force on 7.8 µm beads at different amperages, for both the upper and lower magnets (Figure 13A). For the upper magnet, the force increases linearly with current to 120 pN at 0.2 amps, and any further increase in amperage results in only minor force gains. For the lower magnet, the linear force region extends to about 3.5 pN at 1 amp before plateauing. The difference in behavior between the lower and upper magnets is expected because the lower magnet has a different pole shape and number of wire coils than the upper magnet due to spatial constraints below the chamber. To examine the maximum force for different sized beads, we measured the force at 0.6 amps for beads from 2.8-11 µm in diameter (Figure 13B). This resulted in forces ranging from 32 pN with the 2.8 µm beads, to 260 pN for the 11 µm beads.

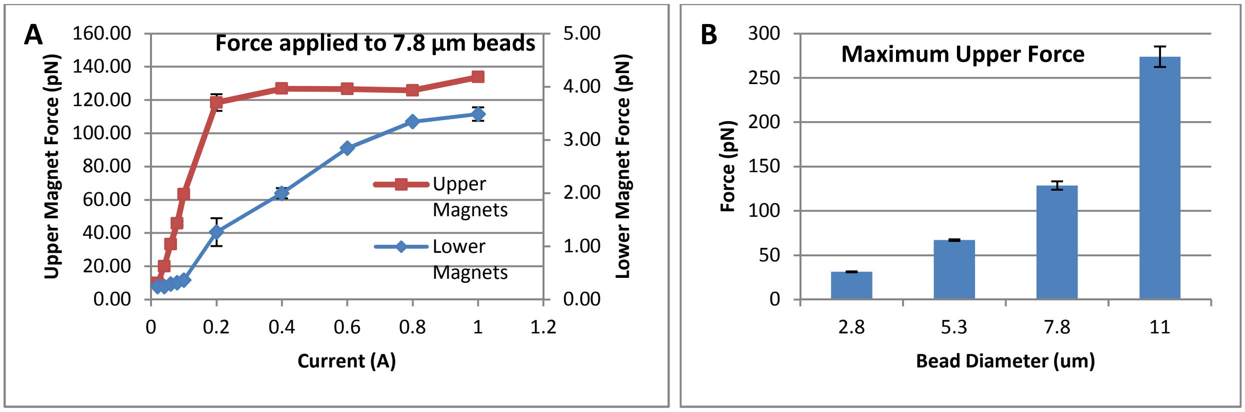

Figure 13: A.) Force on 7.8 µm diameter beads for different levels of current for both the upper and lower magnet. B.) Maximum upward force at 0.6 amps for beads of different sizes. All error bars represent the standard error of the mean (SEM) of two separate data sets of 5-10 beads obtained on different days.

The maximum downward force of 3.5 pN at 1 amps for the 7.8 µm beads allows an estimate of the precision of contact time of the beads with the bottom surface using Equation 11,

$$C_{95} = h * \left[\frac{1}{\frac{F_{down} - 2*COV*F_{down}}{6\pi\mu r}} - \frac{1}{\frac{F_{down} + 2*COV*F_{down}}{6\pi\mu r}} \right],$$

Equation 11

where C_{95} represents the difference in contact time of 95% of the bead population, F_{down} is the force applied with the lower magnet, and COV is the coefficient of variation in force for the beads, and h is the height of the chamber. Using our maximum downward force of 3.5 pN and COV of 0.14 (see Force Variation), we estimate that 95% of beads will contact the surface within 1 second of each other. Equation 2 shows that the contact resolution can be improved by decreasing h or COV, or by increasing F_{down}.

Similarly, the combination of the upward force and spatial resolution controls the bond temporal resolution, or the shortest bond lifetime that can be estimated,

$$\beta_B \approx \frac{6\pi\mu r\eta}{F}, \qquad \text{Equation 12}$$

where β_B is the bond temporal resolution, and η is the spatial resolution. For the 7.8 µm beads, the spatial resolution without reference beads or time averaging is about 75 nm. At the lowest force of 10 pN, the bond temporal resolution is estimated to be 0.5 ms using equation 12. At 100 pN this value decreases to 0.05 ms. Typically, a camera frame rate of 50 Hz is used, and thus we conclude the bond temporal resolution is frame rate limited to 20 ms. A faster frame rate is achievable simply by reducing the pixels per field of view, so higher temporal resolution is possible if some multiplexing may be sacrificed. In contrast, without bead tracking the spatial resolution is estimated as the depth of field (2.78 µm) and the bond temporal resolution at 10 pN becomes 20 ms.

Expanding on the data in Figure 13, the smallest upward force that can be applied using the MMTB is about 2 pN with 2.8 µm beads (data not shown), and is limited by the lowest applicable current of our power supply of 0.02 Amps. This force is about five times smaller than the smallest applicable force using an atomic force microscope [15]. Similarly, the largest force that can be applied with the MMTB is about 260 pN with 11 µm beads at 0.6 Amps (Figure 13B). This force is ~2.5 fold higher the maximum applicable force with an optical trap [15]. This 130-fold force range with commercially available beads is encompasses the forces usually seen when investigating biological phenomena [1-3, 5]. Furthermore, the linear relationship between force and current combined with the ability to program any desired change in current, provides time-dependent force control without the need for a feedback loop. Together, the biologically relevant force range and simple mechanism for manipulating force makes the MMTB a versatile instrument for acquiring constant force measurements.

Force Variation

To assess the variation in force across the field of view, we parsed the field of view into nine sections of 176 x 99 μm per section (Figure 14A, inset), and determined the force on beads within each section at 0.1 amps (Figure 14A). The average force over all the sections is 68 pN, while Section 4 shows the smallest force of 60 pN and section 9 shows the largest force with 74 pN. This range of forces is likely due to a magnetic field gradient that is not perfectly homogenous across the field of view. Changing the magnetic pole tip shape or increasing the space between the magnetic pole tips can help create a more homogenous magnetic field gradient.

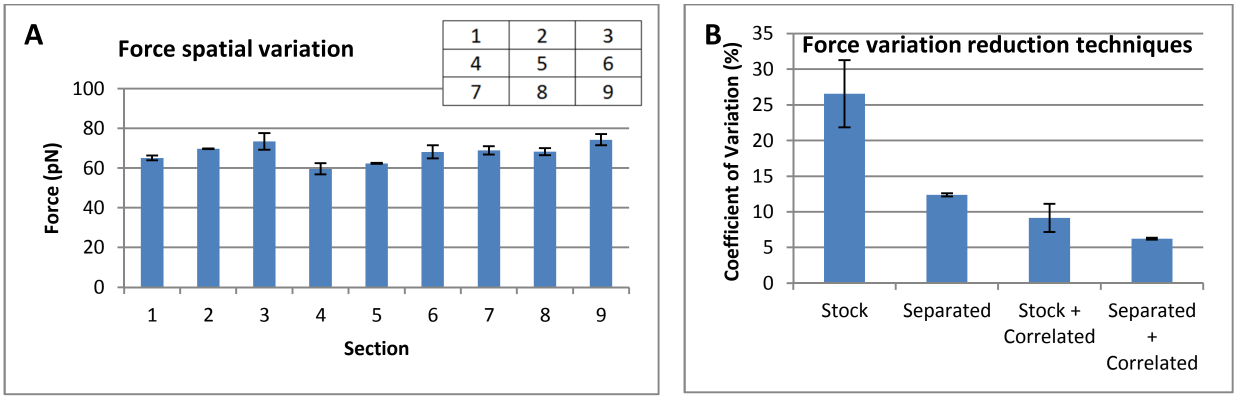

Figure 14: A.) Force applied to 7.8 μm diameter beads in different 176 x 99 μm sections of the field of view (inset). B.) Coefficient of Variation (COV) in force estimations using various techniques. All error bars represent the standard error of the mean (SEM) of two separate data sets of 8-20 beads obtained on different days.

To test the bead to bead force variation, we determined the coefficient of variation (COV) in force of 7.8 μm beads at 0.1 amps. This resulted in a COV of 27% for “Stock” beads: beads directly from the manufacturer’s container (Figure 14B, Stock). We hypothesized that this high value is due to inconsistency in the amount of magnetic material across the bead population, which would result in different bead densities. To test this hypothesis, we separated beads by density using Percoll (p1644, Sigma Aldrich, St. Louis, MO) to create a centrifugal density gradient. We then extracted a small portion of beads from the middle of the density gradient and examined the COV. The separated beads had a 12% COV, less than half the COV of the stock beads.

To further increase the precision of the bead force estimations, we developed a method that correlates the downward force (toward the surface with the lower magnet) and the upward force (away from the surface with the upper magnet). Due to the difference in the amount of magnetic material across the bead population, there is a correlation between the downward force and upward force of individual beads, which can be used to increase the precision of the upward force estimations of adhered beads. This process begins with a calibration step, where the downward and upward force on tens of beads is acquired. The upward force is then modeled as a function of the downward force using a simple linear model. Proceeding pulls, where the beads are initially pulled down to the surface, can then be used to estimate the upward force on beads that have adhered to the surface using the initial downward force. An estimate of the precision in upward bead force can be determined by comparing the linear model to the calibration force measurements, and calculating the standard deviation of the error. This correlation method resulted in a COV of 9% for stock beads, and a COV of 6% for beads that had been separated (Figure 14B). Thus, by combining the separation and correlation methods, the COV is reduced by 78% when compared to stock beads.

Application of MMTB for Single Molecule Force Measurements

To demonstrate the MMTB, we measured the uncoiling and recoiling velocity of type 1 fimbriae from *E. coli* (Figure 15A). We chose this system because it demonstrates the utility of many of the characteristics of the instrument including spatial precision, multiplexing, and bi-directional force control. Type 1 fimbriae have also been studied previously [51, 52, 103] and thus a comparison can be made to measurements taken with more traditional SMFS methods. Briefly, fimbriae are approximately 1 μm appendages found on the surface of *E. coli*. On the tip of each fimbria is the protein FimH, which binds to mannose allosterically [14]. The fimbria itself is made of many helical coils of the subunit FimA and when enough force is applied to the fimbria, the FimA subunits can uncoil sequentially (Figure 15B). If the force on an uncoiled fimbria is reduced sufficiently, recoiling will occur at high velocity. Fimbrial mechanics are a key element in *E. coli's* ability to adhere to mannosylated surfaces under fluid shear stress [104, 105].

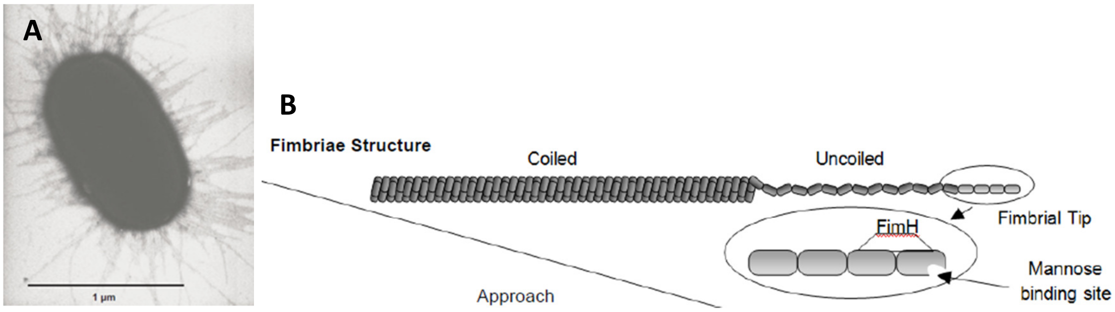

Figure 15: A.) Electron micrograph of *Eschericia coli* (*E. coli*). Figure altered from Thomas [9]. B.) Illustration of fimbria structure. Figure taken directly from Whitfield and Thomas [104].

In our experiment, 7.8 µm carboxyl coated paramagnetic beads were separated by density using Percoll centrifugation, and then covalently linked to Mannose-BSA while fimbriae were non-specifically adsorbed to the glass surface on the bottom of the chamber. Beads, initially near the top surface of the chamber, were pulled down to the bottom surface using the lower magnet, and after approximately one second of contact with the surface pulled away from the surface using the upper magnet. For pulls examining the uncoiling velocity, forces ranging from 46-127 pN were applied to the beads and held for 5 seconds allowing the fimbriae to elongate (Figure 16A). For pulls examining recoiling velocity, after an initial upward force of about 100 pN was applied for 2 seconds to fully extend the fimbria, the force was reduced in a stepwise manner to about 45, 32, and 20 pN respectively (Figure 16B). In this way, multiple recoiling force measurements were made with a single pull. The force on beads that did not adhere to the surface, and thus could be viewed approaching and leaving the surface, were used to create a correlation model of upward force as a function of downward force for different current levels. This model was used to estimate the force on the attached beads. Two data sets from multiple days of experimentation were acquired.

To demonstrate specific adhesion, beads that did not have covalently bound Mannose-BSA were pulled from the fimbria-coated surface at either about 60 or 100 pN. These negative control pulls had less than 1% (SEM = 0.2%) adhesion on average, while the average for beads with Mannose-BSA had 23% (SEM = 5%) of beads adhered to the surface. This demonstrates that the vast majority of adhesive events were bound specifically to the fimbrial tips. Based on the net 22% adhesion rate, a Poisson distribution predicts that 12% of attached beads will form multiple attachments [18].

We used two criteria to ensure that measured velocities were due to uncoiling. First, we used atomic force microscope imaging to ascertain the length of the uncoiled fimbriae, which were found to have an average native length of 0.43 µm with no fimbriae longer than 0.8 µm. We then disregarded any measurements that had bead displacements of less than 1.5 µm during the five second uncoiling pulls, or during the two second 100 pN force for the recoiling pulls. This eliminated any measurements that were only of the reorienting or flipping of the fimbria upright without fimbrial uncoiling, since it is very unlikely that any single fimbria had a length greater than 1.5 um in the native state. Because uncoiling typically extends fimbria to ten times their native length [52], many uncoiled fimbria met this criteria. The second criterion requires at least a 225 nm bead displacement during the time at which the velocity is determined. This second criteria ensures that all velocity measurements are beyond position noise (~75 nm for this experiment).

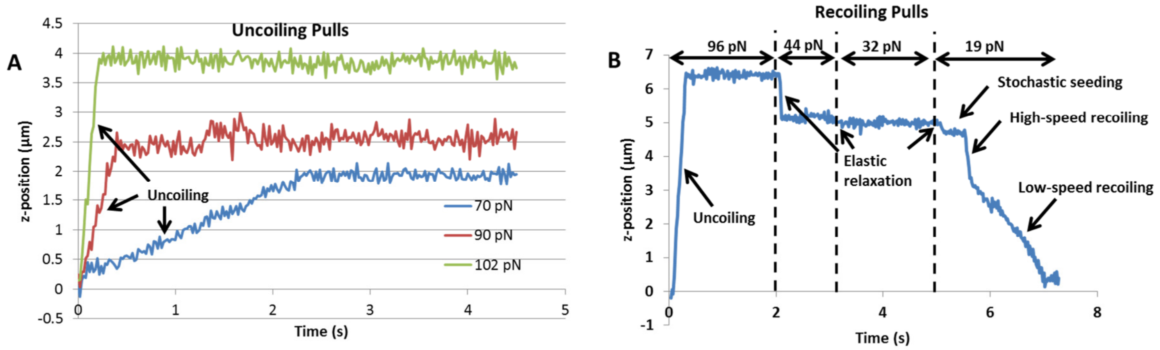

Figure 16: A.) Position data for three uncoiling pulls at different forces. B.) Position data for a recoiling pull.

A key part of the analysis was correctly interpreting the different parts of the displacement curve for recoiling (Figure 16B). The beads are initially pulled away from the bottom surface at high force (~100 pN) to fully extend the fimbria. When the force is lowered, there is an instantaneous relaxation due to the nonlinear elasticity of the fimbria [103]. After the force is reduced to its lowest level (~20 pN), it takes a few tenths of a second before the high-speed retraction begins. We interpreted this as the time it takes for the formation of a nucleation kernel, which has been previously suggested [51]. We found that there were often two speeds of retraction, with the higher velocity always being the initial velocity. This has also been observed previously with type 1 pili, and is hypothesized to be two different methods of recoiling [51]. We used the initial high-speed velocity for the analysis.

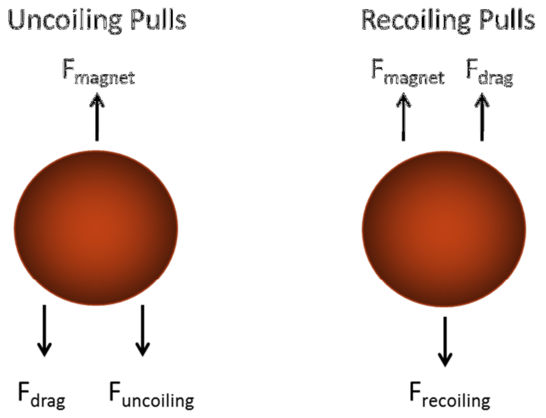

Figure 17: Free body diagrams of forces on the beads during the uncoiling and recoiling pulls.

Lastly, in order to determine the uncoiling forces, the drag force of the bead needed to be taken into account. During uncoiling pulls, the drag force acts in the opposite direction of the force from the magnet (Figure 17). Thus, to determine the uncoiling force, the drag force should be subtracted from the magnet force,

$$F_{uncoiling} = F_{magnet} - F_{drag} \,. \qquad \text{Equation 13}$$

Similarly, for recoiling pulls, the drag force should be added to the magnet force to determine the recoiling force (Figure 17),

$F_{recoiling} = F_{magnet} - F_{drag}$. Equation 14

The drag force can be determined using Equation 10, with lambda estimated using Equation 17 in the Supplementary Materials.

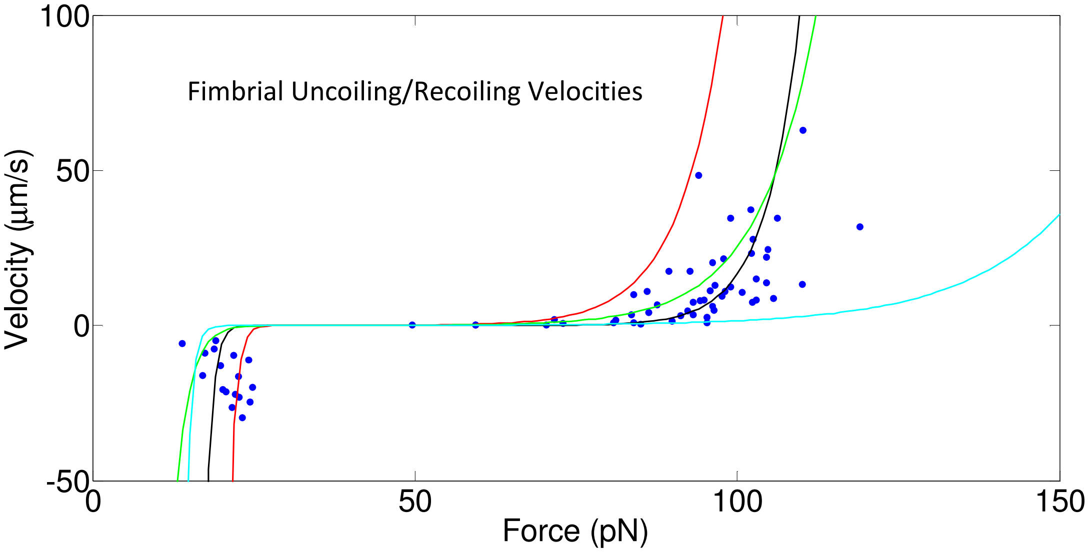

Figure 18: Uncoiling velocity as a function of force. Small blue circles represent the measurements from both data sets. The black line is the best fit model of the aggregate of the two data sets using Equation 15. The red line is the fit of Andersson et al., [51] the green line is the fit of Whitfield et al., [103] and the turquoise line is the fit of Forero et al., [52].

Figure 18 shows the uncoiling and recoiling velocities and their corresponding forces for both of our data sets. Fitting the data from Figure 18 to Equation 15 [52] and using $\Delta L = 5.0$ nm, and $k_b T = 4.114$ pN-nm, resulted in estimates of k_{bal}, f_{bal}, and Δx_u, as shown in Table 3. This model is shown as the solid black line in Figure 18.

$$V(f) = \Delta L k_{bal}\left\{\exp\left[\frac{(f-f_{bal})\Delta x_u}{k_b T}\right] - \exp\left[\frac{(f-f_{bal})(\Delta x_u-\Delta L)}{k_b T}\right]\right\} \qquad \text{Equation 15}$$

To compare our data to previous publications, we also plotted the model fits of Andersson [51], Forero [52], and Whitfield [103], all of whom did similar studies using traditional SMFS methods. These models are shown in Figure 18 as solid lines. At high forces, our model is similar to Andersson and Whitfield, but not Forero, who saw significantly smaller velocities at high force. Considering the recoiling velocities, our model is between the previous studies results. The fit parameters for Equation 15 by Andersson and Forero are shown in Table 3.

Parameter	Our Results (MMTB)	Andersson [51] (Optical Trap)	Forero [52] (AFM)
k_{bal} (s^-1)	.01 ± 0.40	1.2 ± 0.9	2.2
f_{bal} (pN)	31.39 ± 3.73	30 ± 2	22
Δx_u (nm)	0.76 ± 0.32	0.59 ± .06	0.26 ± 0.1

Table 3: Fimbrial uncoiling parameters obtained using Equation 13. Means and errors (SEM) were obtained by fitting our two data sets to Equation 15 separately.

Using the model fit from Equation 15, the degree of data contamination from multiple fimbria attachments can be estimated. The longest fimbria examined using our AFM had a native length of 0.8 µm. If we consider the small probability that two 0.8 µm fimbriae were simultaneously attached to a bead, then the force on the bead would be shared by the two fimbriae, such that each fimbria receives half the total force on the bead. In order to meet the 1.5 µm bead displacement criteria used in our analysis, the two 0.8 µm fimbriae would need to extend 0.7 µm during the five second uncoiling pulls, requiring velocities of greater than or equal to 140 nm/s. According to our model fit for Equation 15, a velocity of 140 nm/s is reached at 75 pN which means a total uncoiling force of 150 pN would be needed to meet the displacement criteria. Since the largest force used in our experiments was 127 pN, we do not expect that any multiple attachment beads met the 1.5 μm bead displacement criteria. Using similar logic, it is even more unlikely that multiple fimbria attachments occurred during recoiling pulls, because recoiling pulls only had 2 seconds at high force, and therefore even higher uncoiling velocities and forces would be required to meet the displacement criteria.

Discussion

Fimbrial Uncoiling Experiments

Previous studies examining fimbrial uncoiling and recoiling have been done with traditional SMFS instruments. This is for good reason, as we are unaware of any other magnetic tweezer besides our MMTB which has the capabilities to complete such a study. However, our MMTB with its unique combination of multiplexing, precision bead tracking, and bi-directional force control was able to efficiently gather single molecule uncoiling and recoiling velocities over a wide range of forces. Without any of the three aforementioned capabilities, this study would have been significantly more difficult.

The multiplexing ability of the MMTB significantly decreased the experimental time needed to acquire the data show in Figure 18. The average time per pull for this experiment was 66 seconds: 6 seconds for the actual pull plus an extra 60 seconds to add new beads to the chamber. Beads cannot be reused for multiple pulls due to attraction between the beads during pulls that causes the beads to aggregate. However, with an average of more than 30 measurements per pull, our measurement rate was estimated to be 0.45 measurements per second. To run a similar experiment with traditional SMFS instruments, there would only be 1 measurement for every 6 second pull, and thus the measurement rate would be 0.17 measurements per second. We therefore estimate that the MMTB is ~2.7 times faster at acquiring data than traditional SMFS instruments for this experiment.

For MT's without precision bead tracking, the spatial resolution is estimated as the depth of field and is on the order of several microns [90]. Since our fimbriae typically uncoiled to lengths of less than 8 µm, many of the uncoiling velocities would have been inaccurate or even undetectable. However, even without using reference beads or time averaging, our spatial resolution of 75 nm was sufficient to determine the uncoiling velocities.

Our novel force correlation method, which required the use of the lower magnet, allowed estimations of force on tethered beads with greatly improved precision, giving us increased confidence in the parameter estimations in Table 3. An alternative method for estimating bead forces uses the Brownian motion of the tethered bead and requires a known tether length and a significant amount of bead position data [106]. This method would have been difficult to implement for the recoiling pulls since the fimbria length was dependent on the bead force, and the bead force was changed every 1-2 seconds resulting in a few data points at each force (Figure 16B).

Lastly, the ability to quickly change the bead force was imperative in estimating recoiling velocities. Because the recoiling velocities are quite rapid, there is a limited time at which force-dependent velocities can be measured. Since we wanted to measure the dependence of this recoiling velocity on force, the force on the beads had to be set quite quickly, otherwise the fimbria could have completely recoiled before the new force level was attained. This was achievable with our electromagnets, where a new steady-state force was reached in ~40 ms, but would be more difficult with permanent magnets where a precise and fast shift in position would be required.

The MMTB

Here we have designed an instrument for gathering single molecule measurements. We specifically designed the MMTB to capitalize on the biggest advantage that MT's have over other SMFS methods: the ability to multiplex. This was accomplished by using a camera with a large field of view, capable of high frame rates at full ROI, and using low magnification objectives. This multiplexing ability allows the acquisition of thousands of single molecule measurements in a single day. Finding the optimal amount of beads to be used can drastically increase throughput. If there are too many beads, diffraction rings will overlap and cause tracking issues, and beads will tend to aggregate more quickly once magnetized. For a discussion on optimal packing density, see Ribeck and Saleh [89].

When choosing the hardware components it is essential to have an understanding of the type of studies that will be done. For precise examination of individual molecules, such as the unfolding of DNA[5], massive multiplexing may not be necessary. In this case it may be valuable to use a camera with a higher frame rate to improve temporal resolution, or use a higher NA objective to improve spatial resolution. Similarly, if experiments do not require precise temporal force control, using more powerful permanent magnets can be advantageous as they allow the use of smaller beads, resulting in greater multiplexing. For our electromagnets, creating a strong and uniform magnetic field gradient was highly dependent on the magnet position and the pole shape. Generally, as one increases the taper of the poles, there is an increase in applied force, but also increased spatial variation of that force. A similar effect occurs as the distance between the poles is decreased. A useful guide for designing high power electromagnets was published by Ishikawa and Chikazumi [100].

One of the most important parameters in SMFS is the precision of position measurements. In experiments extending DNA or unfolding proteins [5, 107], the resolution fixes the smallest change in molecule length that can be detected. When examining bond lifetimes, the combination of resolution and bead velocity determines the shortest bond lifetime that can be measured. The use of one or more reference beads is a simple way of eliminating the effect of stage movement, but requires that beads be firmly adhered to the bottom surface. Time-averaging is another method for improving spatial precision, but at the cost of temporal resolution.

The precision of force estimations is especially important when measuring force induced conformational changes, which are exponentially dependent on force. In the cases where Brownian motion cannot be used to estimate the force on adhered beads, bead to bead force variation can prohibit the accurate estimation of kinetic parameters. The method described here of combining density separation and force correlation improved the precision of force estimations of adhered beads by 78%. To optimize the precision of force estimations, we recommend the methods described above or using beads with uniform magnetic content, which is not guaranteed by uniform size.

There were many tradeoffs considered when designing the MMTB, and these decisions had significant effects on its capabilities. For example, the choice to have a magnet below the chamber increased the contact time resolution and is pivotal for using the force correlation method. However, the lower magnet creates spatial constraints below the chamber and limits acceptable objectives to those with lower NA's, which reduces the spatial precision. Another example is the choice of permanent or electromagnets. Permanent magnets can provide a significantly higher magnetic field gradient [88] which allows the use of smaller beads and increased multiplexing ability. However, permanent magnets don't provide the temporal control of force that was required for examining the recoiling velocities of fimbriae. Similar decisions were made for the shape of the pole tips, the spacing of the poles, the choice of camera, and the beads that were used. Understanding the biological complexes one wishes to study and the types of experiments that will need to be carried out will guide these types of decisions.

Methods

Bead Information

2.8 µm: Dynabead m-280 streptavidin (Thermo Fisher Scientific, Waltham, MA)

5.3 µm: Spherotech PM-50-10 (Spherotech Inc, Lake Forest, IL)

7.8 µm: Bangs Laboratories UM4CN (Bangs Laboratories Inc, Fishers, IN)

11 µm: Spherotech CM-100-10 (Spherotech Inc, Lake Forest, IL)

Model Fit

Equation 15 was fit by minimizing the following error model:

$$\mathrm{E} = \sum_i \frac{1}{\left(\frac{\sigma_f}{E_{f,i}}\right)^2 + \left(\frac{\sigma_v}{E_{v,i}}\right)^2} \qquad \text{Equation 16}$$

Where $E_{f,i}$ is the error in force between the data and the model for the ith data point, and $E_{v,i}$ is the error in velocity between the data and the model for the ith data point. $\sigma_f = 0.07 * F_{i_{data}}$, where $F_{i_{data}}$ is the force for the ith data point, and was determined by examining the residuals from the force correlation model. σ_v = 3.75 µm/s and was estimated by dividing the spatial resolution (~75 nm) by the temporal resolution (20 ms). This error model emphasizes the reduction of the smallest proportional error, either $\left(\frac{\sigma_f}{E_{f,i}}\right)^2$ or $\left(\frac{\sigma_v}{E_{v,i}}\right)^2$. We found that this model resulted in better fits than using the more standard root-mean-squared error model, which emphasizes the reduction of the largest error.

Bead Preparation

In order to bind mannose-BSA to beads, 0.1 mL of 7.8 µm paramagnetic beads (UM4CN, Bangs Laboratories Inc, Fishers, IN) were washed two times in 1 mL of activation buffer (MES hydrate(M8250-25G, Sigma Aldrich, St. Louis, MO) pH 4.5-7.5). After the second wash, the pellet was resuspended in 1 mL of activation buffer and vortexed for 10 seconds. 10 mg of N-Cyclohexyl-N′-(2-morpholinoethyl) carbodiimide methyl-p-toluenesulfonate (C106402-5G, Sigma Aldrich, St. Louis, MO) was added to the beads, vortexed for 10 seconds, and rotated at room temperature for 15 minutes. Beads were then washed 2 times in PBS, and resuspended in 1 mL of the same. The PBS was replaced with 1 mL of mannose-BSA (D-Mannose-BSA, NGP-1108, Dextra Laboratories, UK) in PBS (100 mg/ml) and the solution rotated at room temperature for 2 hours. Beads were then washed in 1 mL of 35 mM glycine (Bio-rad Laboratories, Hercules, CA) with 0.2% BSA (A3059-100G, Sigma Aldrich, St. Louis, MO) and rotated at room temperature for 30 minutes. Beads were then washed and resuspended in 0.2% PBS-BSA and store at 4 °C.

Chamber Preparation

Chamber slides (Fisherbrand Microscope Cover Glass, 24 x 60 x 1.5, Fisher Scientific, Waltham, MA) were placed in Acetone for 3 minutes before being rinsed with ethanol and water. A 100 µl droplet of fimbria in .02% bicarbonate buffer (1.5 µg/ml) was added to center of the bottom slides and incubated for 2 hours at room temperature. A 100 µl droplet of 0.2% PBS-BSA was added to the center of the top slides and incubated at room temperature for 1 hour. Bottom slides were rinsed with 0.2% PBS-BSA three times. Chambers were then assembled with double sided tape and 40 µl of 0.2% PBS-BSA was injected into the chamber via a 100 µl pipet . Chambers were covered and stored overnight at 4 °C.

Percoll Centrifugation

To separate beads by density, 5 ml of 1.5 M NaCl (S271-1, Fisher Chemical, Fair Lawn, NJ) was added to a centrifugation tube. Percoll (p1644, Sigma Aldrich, St. Louis, MO) and water was added to the tube until a density of 1.09 g/ml was reached. Paramagnetic beads were washed 3 times in PBS, and added to the Percoll solution. This solution was then spun at 30,000 x g for 30 minutes. A thumbtack was used to create a hole in the bottom of the centrifugation tube, and the solution was drained into 1 ml aliquots.

Fimbria Preparation

Fimbria production is described in [108].

Supplementary Materials

Stokes Law Corrections Factor λ

When a sphere is moving near a wall or walls, Stokes Law must be corrected for the effect of the walls, typically using a correction factor λ. Figure 19 shows a diagram of the chamber with pertinent parameters used for determining λ. When b/a is large (>15), or when b/(b+c) is small (< 0.2), the effect of the distal wall is insignificant, and lambda can estimated using the empirical approximation for a single wall from [102],

$$\lambda = 1 + 1.08\left(\frac{a}{b}\right) + 1.4\left(\frac{a}{b}\right)^2 . \qquad \text{Equation 17}$$

Considering that our average chamber height is approximately 78 μm, this estimation of lambda was used for estimating forces on 2.8 μm and 5.3 μm beads, where the position of the bead was assumed to be in the middle of the chamber (b = 39 μm). Considering that bead velocities are typically measured in the middle third of the chamber, we estimate that this approximation yields an error in force of less than 5%. Equation 17 was also used to determine the drag force on beads during the fimbrial uncoiling/recoiling experiment, when the beads were near the bottoms surface.

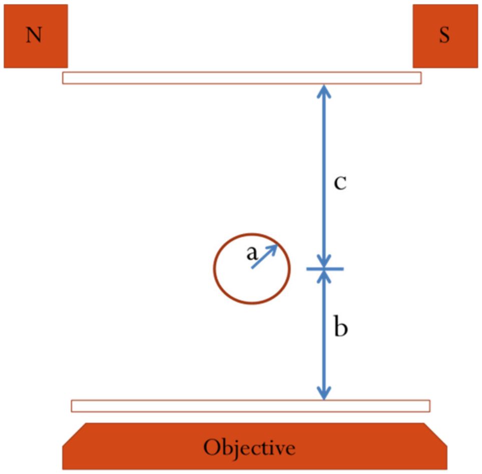

Figure 19**:** Diagram of chamber and parameters used for determining λ.

For the larger 7.8 μm and 11 μm beads, b/a is less than 15, and therefore the second wall has an effect on the bead velocity. In this case, λ can be estimated using the tables and figures created by Ganatos [101]. Values of λ used in Figure 13 ranged from 1.04 for 2.8 μm beads to 1.35 for 11 μm beads.

Chapter 3: The Mechanism of the FimH-Mannose Bond

Abstract

The activated FimH-mannose bond is extremely long lived and forms ideal bonds at forces < 30 pN, suggesting a gateway mechanism that opens at a rate independent of force. Here we study the lifetime of the activated FimH-mannose bond under a large force range using a magnetic tweezers assay. The average lifetime of the bond is > 1000 times that of the biotin-streptavidin bond at low force, making it one of the strongest non-covalent interactions known in nature. The average lifetime is similar between 9 and 30 pN of force, suggesting a force range at which the lifetime is force independent, demonstrating ideal bond behavior for the first time in a natural system. We hypothesize that the long lifetime and ideal behavior is due to a gateway that locks mannose into the binding pocket and opens at a rate independent of force. This study elucidates a mechanism for very strong biological binding, and provides insight into approaches for developing novel antiadhesive therapies.

Background

Receptor-ligand bonds are a fundamental biological mechanism and are used for cell signaling, aggregation, adhesion, and pathogen attachment. Many receptor-ligand interactions have evolved to mediate adhesion under force including bacteria [32], selectins [109-111], integrins [112-115], platelet GPIB [2], cadherins [116, 117], T-cell receptors [118], and fibrin [119]. The structural mechanism for these bonds is not well understood, and is essential knowledge for developing vaccines and antibodies that block adhesion. This antiadhesive therapy development is becoming progressively more important as pathogenic adhesion becomes increasingly drug resistant [11, 120-122].

One such pathogen, uropathogenic Escherichia coli (*E. coli),* is the main cause of urinary tract infections [10] which are estimated to cost $1.6 billion annually in the United States alone [123]. *E. coli* have many appendage-like protrusions known as fimbria (Figure 20A) on the tip of which resides the protein FimH. FimH is a two domain protein (Figure 20B), with the pilin domain anchored to the fimbria, and a mannose-binding lectin domain [124]. FimH-mannose binding has shown similar binding behavior to other receptor-ligand systems and may be a prototype for receptor-ligand binding. These behaviors include allosteric conformation change [9, 125-141], a binding pocket with a gateway or lid [142-153] whose opening has been shown to determine ligand dissociation rates [150, 154, 155], catch behavior [2, 32, 109-119, 130, 135, 136, 156-162], and a mix of short and long lived bonds [41, 114, 133, 157, 160, 163-166]. Thus, understanding the mechanism of FimH adhesion may yield fundamental knowledge of other receptor-ligand bonds, and contribute to the development of novel antiadhesive therapies.

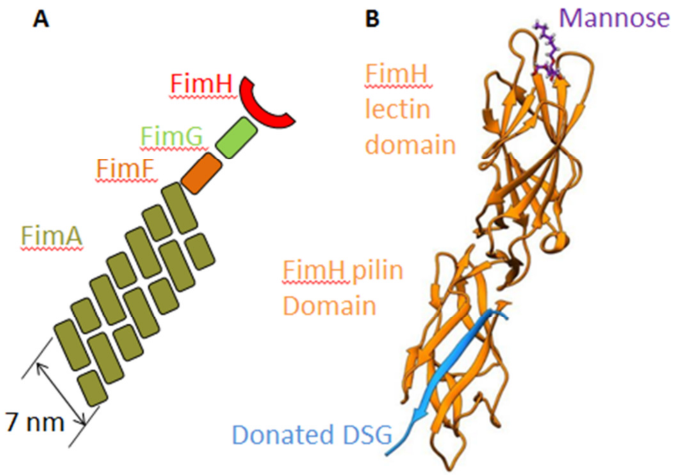

Figure 20: A.) Illustration of fimbria structure. At the tip of the fimbria resides the protein FimH. B.) Cartoon of low affinity FimH structure with donated DSG strand (4XOE).

The FimH-mannose bond is known to form catch bonds [3, 32]: unbinding from a low affinity state at low force, and unbinding from a high-affinity “activated” state at high force. Here we used a magnetic tweezer assay to examine the lifetime of the activated FimH-mannose bond under constant force. Our results show that this bond forms very long lifetimes, with a mean lifetime greater than 15 minutes at less than 30 pN of force. Furthermore, there is a large force range where the lifetime is very similar, demonstrating ideal bond behavior for the first time in a natural system. We hypothesize that the mechanism for these ideal bonds is a gateway that opens at a rate independent of the applied force on the bond. This mechanism is consistent with a four-state model of FimH binding [167], and with recently crystallized structures of FimH conformation states [168].

Results

Lifetime Experiments using a Magnetic Tweezer Assay

To examine the lifetime of FimH binding to mannose, we used a custom built magnetic tweezer assay. This assay facilitates the observation of many bond lifetimes simultaneously, and thus has a significant throughput advantage over more traditional single molecule force spectroscopy methods. In the lifetime experiments, 7.8 µm diameter beads with covalently bound mannose-BSA were suspended in a chamber containing buffer. Magnets below the chamber pulled the beads down to the bottom surface coated with fimbriae from *E.coli* (Figure 21A). After one second of contact with the surface, the beads were pulled away from the surface at high force (70-120 pN) for one second, before the force was changed to a prescribed force and maintained for 886 seconds (Figure 21B). The one second of high force is known as a preload and acts to activate the strong, long-lived state of the bond [3], ensuring that any dissociation was from the activated state and not from the shorter-lived weak state. The position of bound beads was recorded until either bond rupture, signified by a large displacement of the bead, or the maximum time was reached. Two studies of multiple days of data acquisition were performed for sustained forces of 9 pN, 30 pN, 56 pN, and 86 pN.

To acquire high force data, the magnets above the chamber were repositioned to achieve a larger magnetic field gradient, and beads with a higher fraction of magnetic content were used. Using this high force setup, data sets at both 118 and 45 pN of force were taken on separate days. Because of increased bead recruitment and aggregation due to the closer pole position with the high force setup, only 120 seconds of data were acquired for these two forces. The 45 pN data was used to ensure that the changes to the setup did not otherwise affect the results. A 95% confidence interval from a binomial distribution showed that the 45 pN data using the high force setup was not significantly different from the 30 or 56 pN data using the original setup (data not shown). We therefore do not expect that the high force setup had any unintended effects on the data.

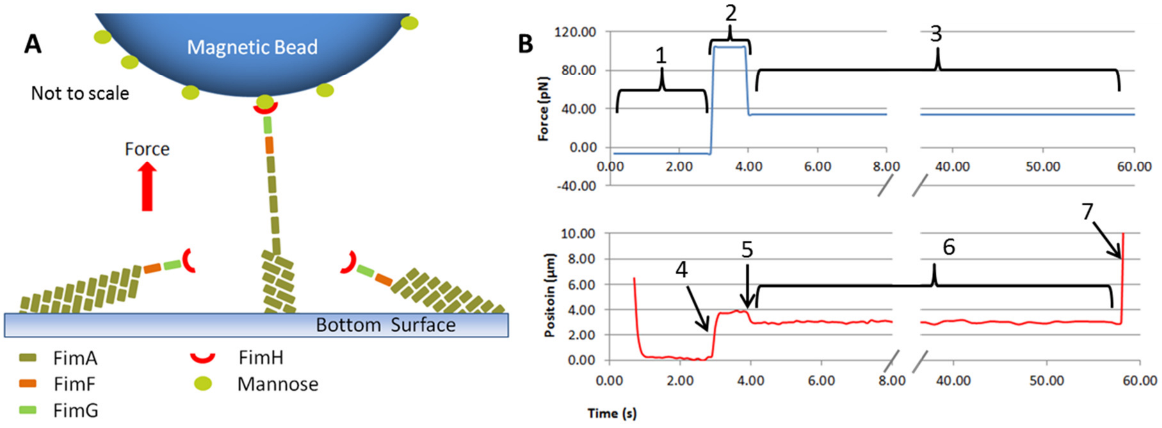

Figure 21: A.) Illustration of a mannose coated bead binding to a fimbria coated surface. Fimbria uncoiled to several times their coiled length under high force. B.) Position and force data for a

single bead. 1) Beads were pulled down to the surface with 5 pN of force. 2) A 70-120 pN preload force was used to activate the bond and extend the fimbria. 3) After the preload, a prescribed force was held for 886 seconds. 4) Fimbria uncoiling. 5) Fimbria elastic relaxation [103]. 6) The bond lifetime was calculated from the end of the preload until bond rupture. 7) Bond rupture was signified by the bead leaving the surface at high velocity.

Testing for Single Bond Behavior

To demonstrate specific, single molecule behavior, we conducted a control experiment in which beads without covalently bound mannose-BSA showed very little adhesion to the fimbriated surface, with an adhesion rate of ~.004, as compared to 0.29 when mannose-BSA was bound to the beads. From this 0.29 adhesion rate, a Poisson distribution predicts that 84% of attachments formed are due to single molecules [18]. In addition, we used a novel mechanical fingerprint of fimbrial uncoiling to ensure that measurements were due to single bonds. In this method, single molecule behavior was signified by > 1 μm total bead displacement, D, during the preload (Figure 21A, 4). Lifetime measurements where D ≤ 1 μm were discarded. The total bead displacement D was the sum of the displacement from the fimbria reorienting upright, d_r, and the displacement from the uncoiling of the fimbria, d_u (Equation 18).

$$D = d_r + d_u \qquad \text{Equation 18}$$

Considering a single fimbria attached to a bead, the maximum displacement of the bead due to reorientation d_r is the coiled length of the fimbriae (Figure 22A). A distribution of the lengths of 39 coiled fimbrial, measured by imaging fimbriae non-specifically bound to mica using an atomic force microscope, showed a length range of 0.2-0.8 μm (Figure 22B). It is therefore likely that additional displacement from fimbrial uncoiling is necessary to meet the 1 μm displacement criteria. At the average preload force of 95 pN, our previous study of fimbrial uncoiling and recoiling predicts an uncoiling velocity of 6.5 μm/s (Chapter 2). Considering that fimbriae can extend up to ten times their coiled length under force [52], and the range of coiled fimbriae lengths in Figure 22B, the displacement due to uncoiling at this average preload force should be 2 μm < d_u < 7.3 μm. The total bead displacement, D, should therefore meet the > 1 μm criteria for a large proportion of the beads within the preload force range.

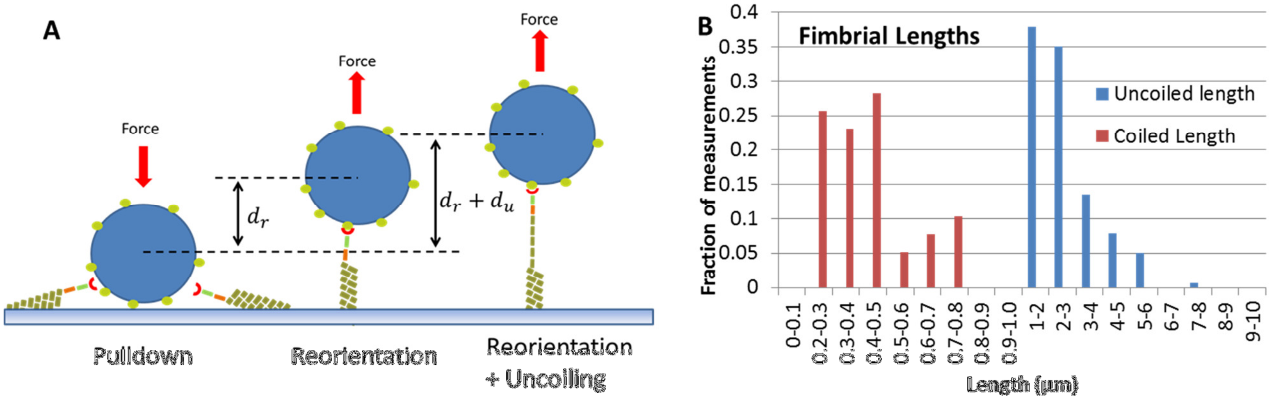

Figure 22: A.) Illustration of the different methods of bead displacement. The total displacement of the bead, D, is the sum of the displacement from reorientation d_r and the displacement from fimbrial uncoiling d_u. B.) Histogram of measured lengths of coiled and uncoiled fimbriae. Coiled lengths were measured by imaging fimbriae on mica using an atomic force microscope. Uncoiled lengths were measured via bead displacement during the preload of lifetime experiments.

For the case of two fimbriae attached to a single bead, the load is shared between the fimbriae, and the effective force on each fimbriae is halved. If we consider the maximum preload force applied of 120 pN, each fimbria is therefore subjected to a 60 pN load. Due to the exponential dependence of force on uncoiling velocity, at 60 pN the uncoiling velocity is only expected to be

10 nm/s, and the displacement due to uncoiling, d_u, is 10 nm. In this case, for D to be greater than 1 µm, the displacement due to reorientation, d_r would need to be greater than 990 nm. This means that two fimbriae longer than the longest measured coiled fimbriae would need to be attached to the bead simultaneously, since d_r is limited by the shortest attached fimbria. A conservative estimate of the likelihood of such an event can be estimated by using a binomial distribution to predict the probability of randomly finding two fimbriae of greater than 0.8 µm in length, for the coiled length distribution in Figure 22B. Using a 95% confidence interval, this probability is .008 for two fimbriae, and .0007 for three fimbriae. Again, these probabilities are very conservative, and we therefore expect that any multiple fimbriae attachments were eliminated from the analysis.

Examining the Data

If we consider the fraction of bonds surviving as a function of time $S(t)$, then $\frac{dS(t)}{dt} = -k * S(t)$, where k is the off rate for a single force with units of inverse seconds. From this, a solution for $S(t)$ is

$$\ln(S(t)) = -k(f) * t \qquad \text{Equation 19}$$

This means that for a simple bond with a single state, the off-rate at force f, $k(f)$, is equal to the negative of the slope of the natural log of the fraction of bonds surviving over time. Furthermore, the average bond lifetime at a single force is equal to $\frac{1}{k(f)}$.

Using Equation 19 as guide, we determined the fraction of bonds surviving as a function of time for each force from the lifetime experiments (Figure 23A). At the two lowest forces of 9 and 30 pN, a large fraction of bonds lasted longer than the experimental duration of 886 seconds, indicating a very long average lifetime. Also, these two lowest forces resulted in comparable slopes, suggesting that the off-rate and average lifetime were similar between the two forces. This indicates that at low force the FimH-mannose bond average lifetime is independent of force. A bond with a force independent average lifetime is known as an ideal bond and has never before been demonstrated in natural system. As the force increases beyond 30 pN, the off-rate increases until the largest force of 118 pN. This increase in off-rate with increasing force corresponds to a decrease in the average lifetime of the bond. A bond whose average lifetime decreases with force is known as a slip bond.

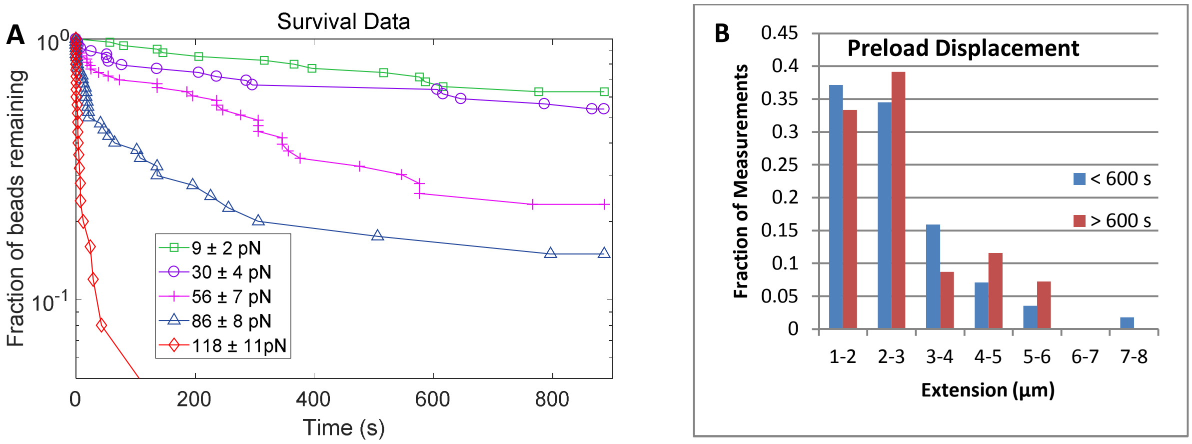

Figure 23: A.) Fraction of bonds surviving over time from the lifetime experiments. B.) Histogram of preload displacements for bonds lasting < 600s and bonds lasting > 600 s.

At forces greater than 30 pN, the data in Figure 23A shows that the longest lived data has a different slope than the shortest lived data. This indicates that there are at least two off-rates, and thus lifetimes, at these forces. One possible explanation for this could be that the longer lived bonds were subject to different force conditions than the shorter lived bonds. To examine this, we compared the prescribed force and preload force for bonds lasting less than 600 seconds to those lasting longer than 600 seconds for the 56 and 86 pN forces (Figure 26, Supplementary

Materials). Both the prescribed force and preload force showed very similar values for the shorter and longer lived bonds and thus the force conditions does not explain the bond behavior. Another explanation for the long lived bonds at 69 pN could be that these beads had multiple fimbriae attachments. This is investigated below.

The preload displacement criteria discussed earlier should have eliminated the presence of multiple bond attachments from our data sets. To ensure that this is the case, we examined the preload displacement distribution for bonds lasting less than 600 seconds, and bonds lasting longer than 600 seconds (Figure 23B). If a bead has more than one fimbria attached, the force on each bond will be reduced, since the force on the bead is divided amongst the fimbriae. The reduced force on each fimbriae will decrease the uncoiling velocity and thus the displacement due to uncoiling d_u. Therefore, if there is a prevalence of multiple fimbriae attachments, the longer lived bonds should have a higher proportion of small preload displacements than the shorter lived bonds. Examining the distribution in Figure 23B, there is very similar distribution in preload displacements between the short and long lived bonds. Furthermore, both short and long lived bonds show a significant proportion of displacements greater than 2 μm. These large displacements must be due to fimbrial uncoiling since all measurements of uncoiled fimbriae were less than 0.8 μm in length. Thus, the distribution of preload displacements in Figure 23B is inconsistent with the presence of multiple fimbriae attachments.

Another possible explanation for the different off-rates at forces greater than 30 pN is that there are different types of mannose in the mannose-BSA that was used. Some of these populations of mannose may bind more strongly to FimH than others, resulting in multiple off-rates. Because the number of different types of mannose within the mannose-BSA is unknown, this is very difficult to assess quantitatively. Lastly, there could also be multiple conformational states within the activated state of the FimH-mannose bond. This would also result in the multiple off-rates seen in Figure 23A.

In summary, the lifetimes of the activated FimH-mannose bond were longest at the two lowest forces of 9 and 30 pN, with nearly half of bonds surviving the full 886 seconds (Figure 23A). The similar lifetimes at these two forces is novel behavior for a physiological system and is indicative of an ideal bond. As the force increased beyond 30 pN there was a transition to slip bond behavior, where the average lifetime of the bond decreased with force. The multiple slope behavior of the bonds at greater than 30 pN cannot be explained by different force conditions, is unlikely to be due to multiple bonds, and may represent more complex bond behavior than predicated from Equation 19. Due to this, in the proceeding analysis, we only examined the shortest lived 75% of the data, which eliminates most of the secondary slope behavior in Figure 23A.

Fitting Models to the Data

To fit a model to the data in Figure 23A, we considered both a slip model and a model combining ideal behavior and slip behavior. From Bell's equation [13], a slip model for unbinding can be described by

$$k(f) = k_{slip} * \exp(\frac{F * x_{slip}}{k_b T}), \qquad \text{Equation 20}$$

where $k(f)$ is the force-dependent off-rate, k_{slip} is the slip off-rate at zero force, F is the applied force to the bond, x_{slip} is the distance coordinate in the direction of force, and $k_b T$ is the

Boltzmann constant times temperature. For the ideal + slip model, a force independent off-rate, k_{ideal}, was added to Equation 20 such that

$$k(f) = k_{ideal} + k_{slip} * \exp(\frac{F * x_{slip}}{k_b T}) \qquad \text{Equation 21}$$

To compare the two models, we fit Equations 20 and 21 to the data in Figure 23A, with the fits shown in Figures 24A and 24B. The slip model shows good agreement with the 9 pN data, but shows large errors for the majority of the 30 pN data. This deviation from the data is expected from the slip model, since the slip model requires an exponential increase in off-rate with force, while the data shows a very similar off-rate at 9 and 30 pN. The slip model also fails to fit the data at the 56 and 118 pN forces. Comparatively, due to its force-independent off-rate, the ideal + slip model was able to simultaneously fit both the 9 and 30 pN force data. The slip + ideal model matches the majority of high force data as well.

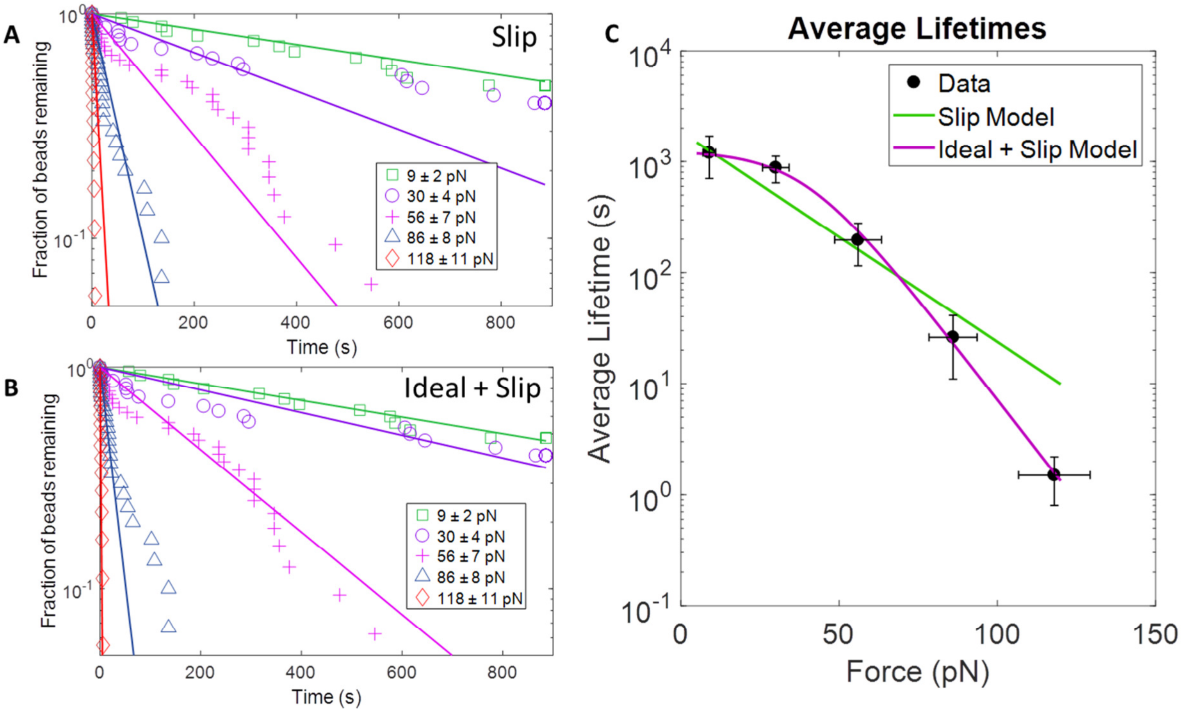

Figure 24: A) Slip model fit to the data. Parameters from fit were $k_{slip} = 5.4 * 10^{-4}\ s^{-1}$, and $x_{slip} = 0.179\ nm$ B) Ideal + Slip model fit to the data. Parameters from fit were $k_{ideal} = 8.0 * 10^{-4} s^{-1}$, $k_{slip} = 3.1 * 10^{-5}\ s^{-1}$, and $x_{slip} = 0.346\ nm$ C) Average lifetime as a function of force for the data,Slip model fit, and Ideal + Slip model fit. Error bars represent the standard deviation of two separate data sets obtained on different days.

To estimate the average lifetime of the FimH-mannose bond from the data, we fit Equation 19 to each force and determined the average lifetimes by using the inverse of the estimated off-rates (Figure 27, Supplementary Materials). These estimates of the average lifetime for the data are shown in Figure 24C, along with the calculated average lifetimes for the slip model fit and ideal + slip model fit. The lifetimes at the two lowest forces are 1199 and 880 seconds for the 9 and 30 pN forces respectively, and are not significantly different from each other. For contrast, the average lifetime of the biotin-streptavidin bond, considered one of the strongest non-covalent interactions, is ~ 1 in this same force range [84]. Thus, the lifetime of the FimH-mannose bond is extremely long lived, and shows similar lifetimes at low forces.

Figure 24C demonstrates that the slip model does not have the same lifetime trend as the data. When viewed on a logarithmic scale, the lifetimes for a slip model are linear, due to its exponential relationship between lifetime and force. However, the lifetimes for the data clearly do not follow a linear trend in Figure 24C. Due to this disagreement, the lifetimes from the slip model cannot match the lifetimes from the data at all forces. This deviation between the slip model and the data is most keenly observed at 118 pN, where the slip model predicts a lifetime of 11 seconds while the data has an average lifetime of 1.5 ± 0.7 seconds. In contrast, the lifetimes from the ideal + slip model show a very similar shape to the data and is within one standard deviation of the data at all forces.

Figure 24 demonstrates that a slip bond model cannot explain the data from the lifetime experiments. This is shown by discrepancies between the slip model fit and the data in Figure 24A and is also observed in Figure 24C, where the exponential decrease in lifetime with force prevents the slip model from matching the lifetimes from the data. However, by adding a force independent off-rate, k_{ideal}, an ideal +slip model shows agreement with data in Figure 24B, and is within error of the data at all forces in Figure 24C. The superiority of the ideal + slip model provides further evidence that the FimH-mannose bond forms ideal bonds at low force.

Discussion

Until recently, the only known conformations of FimH were a short-open state, where the mannose pocket, or gateway, was open and the interdomain region between the lectin and pilin domain was compressed, and a long-closed state where the gateway was closed and the interdomain region was elongated. However, Rodriguez et al., created a FimH mutant that simultaneously showed low affinity for mannose, yet bound an antibody that recognizes the elongated interdomain region [167]. This demonstrates that the gateway and interdomain region may only be loosely coupled and that there may be intermediate states of FimH. Sauer et al., provided further evidence for this hypothesis by crystallizing a third “short-closed” state [168] of FimH bound to mannose. Based upon this evidence, and the data from this study, we hypothesize that there are actually four states of FimH as shown in Figure 25A. The two primary states are the short-open and long-closed states as previously described. There are also two intermediate states: the short-closed state which has a short interdomain region and closed gateway, and a long-open state which has a long interdomain region and an open gateway. When combined, these four states create a force dependent cycle. The key feature of this model is that the rate at which the gateway opens is independent of the applied force, resulting in the ideal behavior seen at low forces in our experiments.

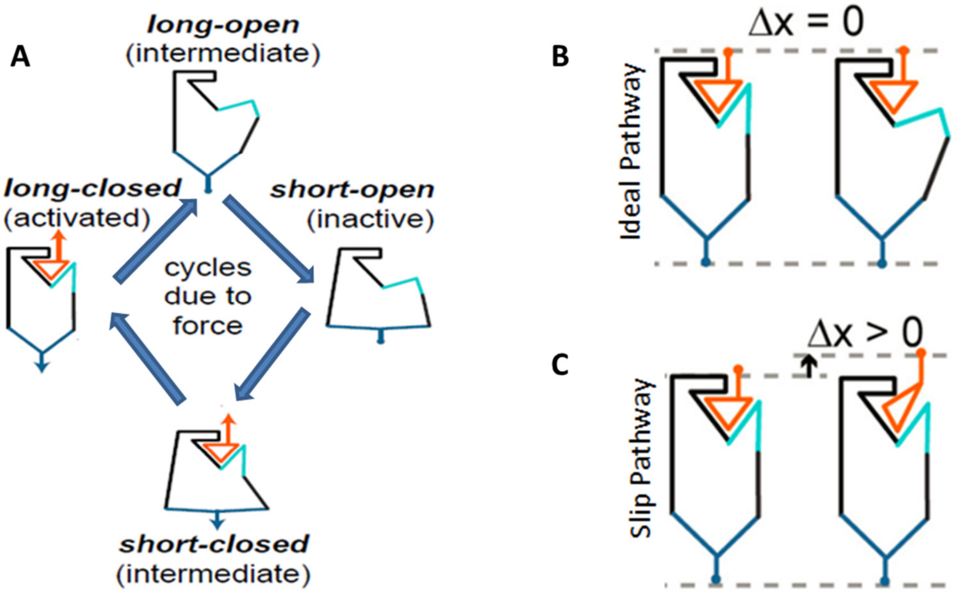

Figure 25: A.) A schematic of the four-state model of FimH binding. B.) Schematic of the ideal pathway for unbinding. C.) Schematic of the slip pathway for unbinding.

During our experiments, the preload acted to convert all the bonds into the long-closed state. Because force was maintained on the bond throughout the experiment, FimH could not unbind through the short-closed to short-open pathway, because force keeps the interdomain region in the elongated form. Thus, the bond must unbind via the long-open state. Because the gateway acts orthogonally to the direction of force, there is no length change in the direction of force when the gateway opens, and thus Δx = 0 (Figure 25B). This long-closed to long-open pathway represents the ideal behavior seen at less than 30 pN. Ideal bond behavior has only been demonstrated previously with a non-physiological variant of cadherins exhibiting a very short lifetime [117]. In contrast, our experiment examined wild type FimH with extremely long-lived ideal behavior.

At higher forces, we hypothesize that the slip behavior is due to a repositioning of mannose in the gateway, such that it can then slip out while the gateway is closed, resulting in $\Delta x > 0$ (Figure 25C). This repositioning has been shown in simulations when mannose has been under high tensile force, and was found to have a reduced lifetime when compared to the original mannose orientation [169]. Therefore, the two unbinding pathways are a long lived ideal pathway dependent on the rate of gateway opening, and a slip pathway that occurs at higher force when the mannose is repositioned in the pocket.

This four-state hypothesis supports the ideal + slip model used to fit our data. While the ideal + slip model shows agreement at most forces, it does not account for the longer lived bonds at forces greater than 30 pN. We feel confident that these were not multiple bond interactions, as our procedure used a combination of low attachment probability and the bead displacement to ensure measurements were due to single bonds (Figure 22A). We also examined the distribution of bead displacements during the preload, and did not see any difference between short and long lived bonds (Figure 23B). Lastly, we examined the force conditions between short and long lived bonds for the 56 and 86 pN forces and did not see any significant differences (Figure 26, Supplementary Materials). We therefore conclude that there is likely more complexity in the unbinding of the FimH-mannose bond at high force than has been considered here. Yet, we reiterate that this complexity does not negate our main findings that the FimH-mannose bond is extremely long lived, and shows ideal bond behavior at less than 30 pN of force.

Our experimental results and the four-state hypothesis have significance on multiple fronts. First, they provide guidance for developing antiadhesive therapeutics that wish to block pathogenic adhesion. Our model suggests that therapeutics that target the regulatory region of FimH, attempting to allosterically maintain the open gate may not be effective since they will be competing with force. However, therapeutics which keep the gate open by targeting the gateway may be more successful. This study also provides insight into the force conditions at which therapeutics should be tested, which we found to be a large force range. More generally, this study elucidates a mechanism for strong and long-lasting binding: a gateway whose rate of opening is unaffected by force. As discussed in the introduction, the FimH-mannose bond shares many characteristics with other biologics, and may therefore have a similar binding mechanism. Since biological adhesion is an extremely important mechanism for homeostasis and development, we consider the understanding of the mechanism of the binding to be valuable.

Methods

Bead Preparation

0.1 mL of 7.8 µm paramagnetic beads (UM4CN, Bangs Laboratories Inc, Fishers, IN) were washed two times in 1 mL of activation buffer (MES buffer pH 4.5-7.5). After the second wash, the pellet was resuspended in 1 mL of activation buffer and vortexed for 10 seconds. 10 mg of WSC (Water soluble carbodiimide) was added to the beads, vortexed for 10 seconds, and rotated at room temperature for 15 minutes. Beads were then washed 2 times in PBS, and resuspended in 1 mL of the same. The PBS was replaced with 1 mL of mannose-BSA in PBS (100 mg/ml) and the solution rotated at room temperature for 2 hours. Beads were then washed in 1 mL of quenching solution (30-40 mM glycine with 0.2% BSA), and rotated at room temperature for 30 minutes. Beads were then washed and resuspended in 0.2% PBS-BSA and store at 4 degrees C.

Bead Tracking

Experimental images were analyzed using a custom Matlab script (MathWorks, Natick, MA) similar to other particle tracking algorithms [22, 91]. Before each experiment a lookup table was created which determines a radial intensity vector of a representative bead at different z-positions by moving the objective small axial steps while the beads are stationary. During the experimental pulls, when the beads are moving and the objective is stationary, the radial intensity vectors of all the beads in the field of view were extracted and compared to the lookup table to estimate their z-positions.

Chamber Preparation

Chamber slides (Fisherbrand Microscope Cover Glass, 24 x 60 x 1.5, Fisher Scientific, Waltham, MA) were placed in Acetone for 3 minutes before being rinsed with ethanol and water. A 100 µl droplet of fimbria in .02% bicarbonate buffer (1.5 µg/ml) was added to center of the bottom slides and incubated for 2 hours at room temperature. A 100 µl droplet of 0.2% PBS-BSA was added to the center of the top slides and incubated at room temperature for 1 hour. Bottom slides were rinsed with 0.2% PBS-BSA three times. Chambers were then assembled with double sided tape and 40 µl of 0.2% PBS-BSA was injected into the chamber via a 100 µl pipet . Chambers were covered and stored overnight at 4 degrees C.

Percoll Centrifugation

To separate bead by density, 5 ml of 1.5 M NaCl was added to a centrifugation tube. Percoll (p1644, Sigma Aldrich, St. Louis, MO) and water was added to the tube until a density of 1.09

g/ml was reached. Paramagnetic beads were washed 3 times in PBS, and added to the Percoll solution. This solution was then spun at 30,000 x g for 30 minutes. A thumbtack was used to create a hole in the bottom of the centrifugation tube, and the solution was drained into 1 ml aliquots.

Fimbria Preparation

Fimbria production is described in [108].

Model Fitting

Slip and Ideal + Slip models were fit by reducing the proportional error between the model and the data from the lifetime experiments as defined in Equation 22.

$$E_p = \sum_j \sum_i [(L_{i,j} - M_{i,j})/(\sigma_j)]^2 \qquad \text{Equation 22}$$

Where E_p is the total proportional error, $L_{i,j}$ is the fraction of bonds surviving after time-point i in force bin j from the data, $M_{i,j}$ is the corresponding fraction of bonds surviving using Equation 20 for the slip model and Equation 21 for the ideal + slip model, and σ_j is the standard deviation of the force in force bin j.

Average Lifetime Estimates

For each of the two studies of FimH-mannose lifetimes, the data at each force was fit with an exponential decay model (Equation 19), and an estimate for the off-rate was determined by minimizing the error in Equation 23.

$$E_{r,j} = \sum_i [(L_{i,j,r} - M_{i,j,r})]^2 \qquad \text{Equation 23}$$

Where $E_{r,j}$ is the error for study r at force j, $L_{i,j,r}$ is the fraction of bonds surviving after time-point i in force bin j from the study r, $M_{i,j,r}$ is the corresponding fraction of bonds surviving from Equation 19. The average lifetime was determined using

$$\boldsymbol{L_j} = \left(\frac{\boldsymbol{N_{1,j}}}{\boldsymbol{k_{1,j}}} + \frac{\boldsymbol{N_{2,j}}}{\boldsymbol{k_{2,j}}}\right)\frac{\boldsymbol{1}}{\boldsymbol{N_{1,j}+N_{2,j}}}. \qquad \text{Equation 24}$$

Where $N_{1,j}$ is the number of bonds examined in study 1, in force bin j, and $k_{1,j}$ is the off-rate for study 1 for force bin j, determined by minimizing Equation 23. $N_{2,j}$ and $k_{2,j}$ are the corresponding number of bonds examined and the off-rate for study 2.

The lifetimes for the slip and ideal + slip models was determined by taking the inverse of the force-dependent off-rates, $k(f)$, from the fits determined using Equations 22.

Supplementary Materials

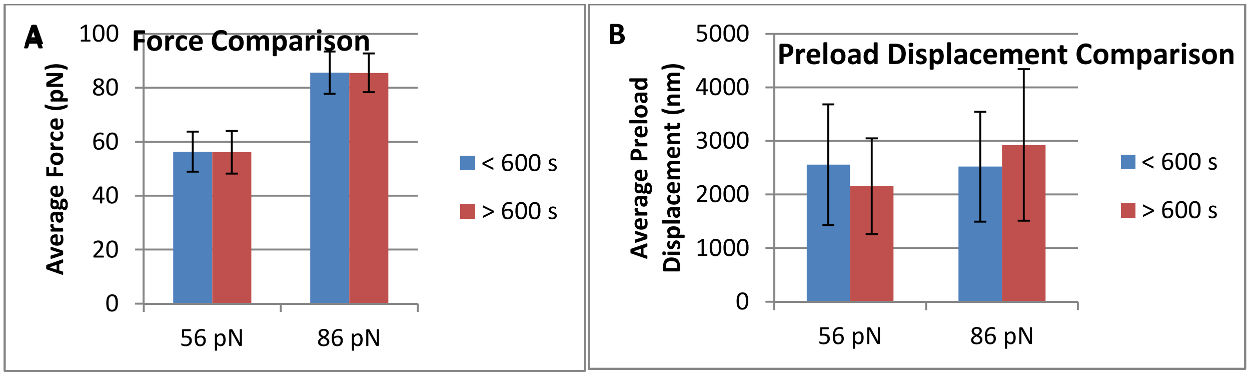

Figure 26: Comparison of bonds lasting < 600 s to those lasting > 600s A.) Prescribed force. B.) Preload force.

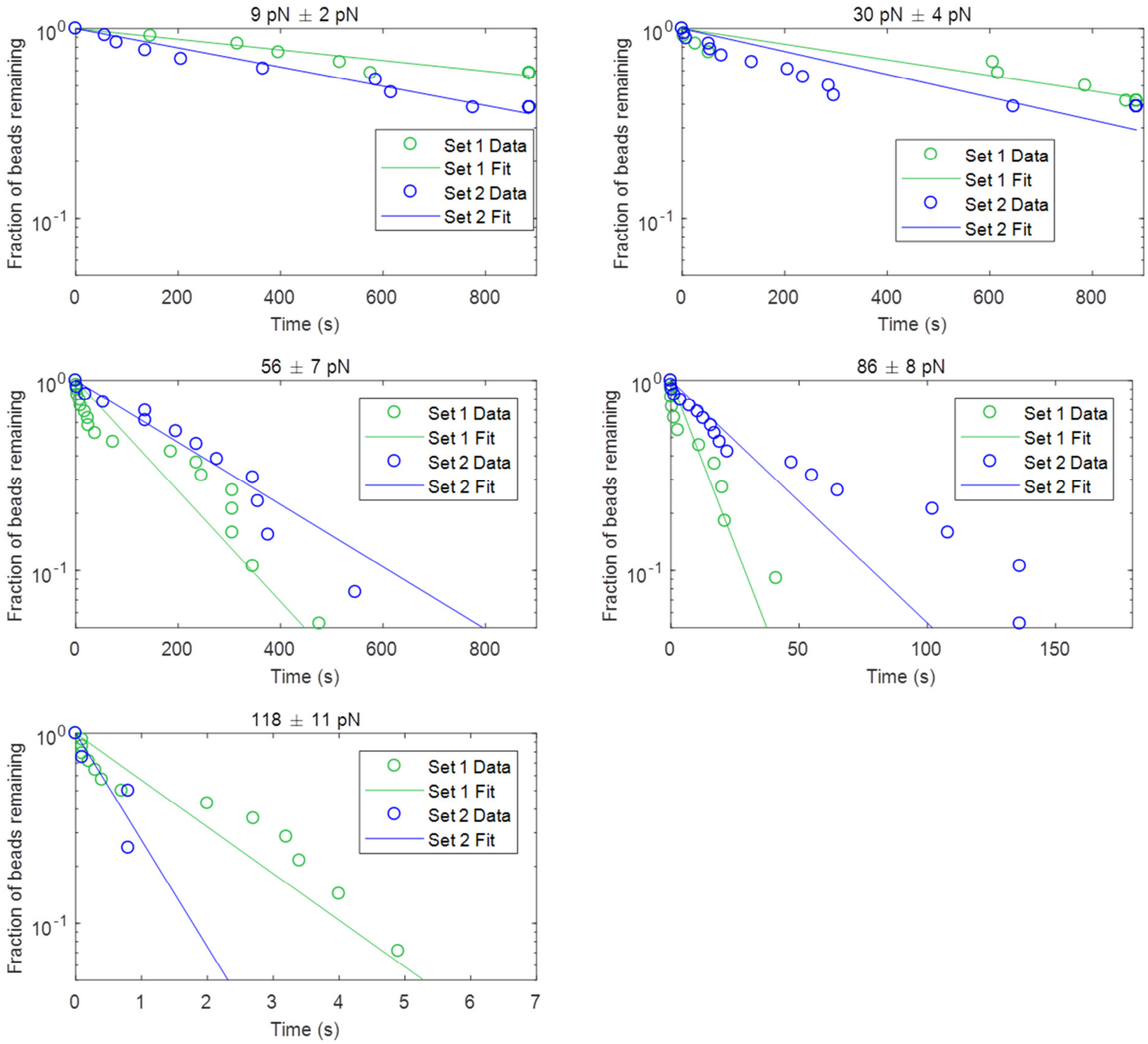

Figure 27: Lifetime fits for each force.

Conclusions and Future Work

Single Bond Methods

The first contribution of this dissertation is the review of SMFS single bond methods. Since SMFS is a relatively recent development, first appearing in the early 1990's, it is not surprising that some of the methods used in the early studies have now been shown to provide inaccurate results. Unfortunately, those methods which have been found to be the most effective at reducing the effect of multiple bonds all have drawbacks. Reducing the adhesion rate also decreases the data acquisition rate, and therefore increases experimental time. The ability to functionalize surfaces such that only single molecule interact, shows great promise for ensuring that only single bonds can form, but has not yet been demonstrated. Using probe oscillations requires large amount of position data to create accurate histograms, and therefore may not be feasible for bonds with short lifetimes. Mechanical fingerprints require adding a linker or marker molecule to the binding construct, and therefore requires expertise in protein engineering, and increases the complexity of data analysis. Lastly, most of the multiple bond models have yet to be fully proven, and the one that has is only applies to homodimers.

Perhaps the most interesting area for future work in the area of single bond methods is the functionalization of surfaces such that only single molecules can interact. This would ensure that only single bonds can form, and would not require a low adhesion rate or complex data analysis. One method of creating single molecule interactions is using regularly spaced arrays, which has the added benefit of significantly increasing the multiplexing ability of a magnetic tweezer [21]. Unfortunately, this method of creating arrays via microetching does not guarantee that each spot in the array is a single molecule, and so multiple bonds can still form. An alternative approach is through the use of DNA origami. These techniques have already been used to create arrays on the order of microns in size, and can have regularly spaced attachment points for single molecules [170-175]. It therefore seems that all the components are available to create an array that ensures single molecule interactions.

The MMTB

In chapter 2 I described the capabilities of our MMTB and demonstrated its application by examining the uncoiling and recoiling velocities of type 1 fimbriae from *E. coli*. This examination highlighted the utility of the main capabilities of the instrument. First, even though these pulls lasted less than ten seconds, the ability to examine up to 30 paramagnetic beads simultaneously increased the rate of data acquisition by nearly three times. The tracking algorithm provided spatial resolution of 75 nm for the 7.8 μm diameter beads, allowing precise measurements of bead velocities. This would have been difficult using a depth of field resolution, which is estimated to be 2.78 μm, since the velocity measurements were taken within a few microns of the surface. Because fimbria uncoiling and recoiling velocities are very sensitive to force, the force had to be changed quickly to ensure accurate velocity measurements. The choice of electromagnets was imperative to achieve this, as the magnets are able to achieve a new steady force in 40 ms. Lastly, having a magnet below the specimen was important not only for allowing reproducible contact times of the beads with the surface, but also significantly improved the precision of force estimations on adhered beads using the force correlation method.

While the MMTB provides a combination of abilities that has not been demonstrated before to my knowledge, I believe there are many improvements that can be made. Most importantly, a stronger magnetic field would allow the use of smaller beads, which would result in more beads within the field of view. This could be achieved by using larger diameter magnetic poles, with a more optimally shaped tip, and using more wire coils. It seems quite possible that such an electromagnet could provide a significantly stronger magnetic field without sacrificing field uniformity across the field of view. If this larger magnetic pole setup could be used for the lower magnet as well, the increased strength of the field would not require that the poles be placed so close together, which currently limits the MMTB to objectives with longer working distance and lower NA. Thus, if the lower poles could be placed further apart, a higher NA objective could be used and the spatial resolution increased.

There are two more improvements which could drastically increase the throughput of experiments. First, a significant fraction of experimental time is currently wasted between pulls by the need to remove the chamber from the instrument, inject new beads, and then reinser the chamber into the instrument. This is a required step due to beads aggregating together under the effect of the electromagnetic field. This step could be automated by installing a flow device which flows a mixture of beads and buffer through the chamber at high flow rates, thus washing out any old beads that have aggregated together or are still attached to the surface, and adding new beads. Instead of the 60-90 seconds required using the current method, a flow system could achieve this in a matter of seconds or less. Secondly, the technique of immobilizing biomolecules to the surface via hexagonal arrays as opposed to random spacing has been shown to increase the amount of trackable beads by tenfold [21]. While this technology is relatively new, and it is uncertain as to how viable the immobilization of *single* biomolecules is, this has the potential to drastically increase the throughput for a magnetic tweezer.

Each of the improvements described above has already been demonstrated, and therefore a combination of them is entirely possible. Such an instrument would be capable of simultaneously examining > 500 beads simultaneously, with ~1 nm of spatial precision, and provide a large force range of up to hundreds of piconewtons. This instrument could also be entirely automated. A researcher could insert a chamber, connect a large volume of beads and buffer to the flow system, program in the desired force and flow conditions, and have the instrument run for hours or days without need for human interference. The results from the experiment, already organized into tables and figures, could be waiting for the researcher upon his or her return. The scope of potential studies with such an instrument is considerable, and is, again, entirely possible with today's technology.

The lifetime of the FimH-mannose bond

In Chapter 3 I examined the lifetime of the activated FimH-mannose bond under a range of forces. Using a novel mechanical fingerprint of fimbrial uncoiling, I demonstrated that at low forces the FimH-mannose bond is very long lived with a lifetime greater than 1000 times longer than the biotin-streptavidin bond at similar forces. Furthermore, the lifetime is nearly constant at forces of less than 30 pN, demonstrating ideal bond behavior for the first time in a natural system. Above 30 pN, the average lifetime decreases with increasing force, with the shortest average lifetime of 1.5 seconds at 118 pN of force. It was found that a model combining the behaviors of an ideal bond and a slip bond fit the data better than a slip bond model, providing further evidence that the FimH-mannose bond forms ideal bonds at low force. Finally, it was hypothesized that the mechanism for the ideal behavior is a gateway that opens at a rate independent of force.

Perhaps the greatest challenge of this project was the extremely long lifetime of the bond. Even with a pull lasting a fifteen minutes, almost 50% of bonds were still attached at less than 30 pN of force. These long pulls made the acquisition of enough bond breaks very time intensive. And while it seems that I was able to acquire enough breaks to get a clear picture of the dependence of lifetime on force, having more data would have been beneficial. Also, it would be interesting to investigate the lifetime at forces very near 0 pN, to see if the ideal + slip model still holds true. This would not have been possible with the construct I used in these experiments, since some force is required to maintain the activated state. However, using the isolated lectin domain of FimH, which shows very similar behavior to the activated state of full FimH, these types of measurements would be possible. Further investigation of the double-exponential behavior seen at forces greater than 30 pN may also be important to fully understand the mechanism of the FimH-mannose bond. This behavior is unexpected for a single state bond, and does not fit our ideal + slip model. Examining similar forces with the isolated lectin domain variant would again be helpful and would elucidate whether this behavior could be due to allosteric contributions from the interdomain region. Also, performing similar experiments with an AFM would show whether or not this behavior could be an artifact of the MMTB experiments.

One of the motivations for this experiment is that the FimH-mannose bond has similar behavior with other bacteria that cause a variety of diseases. Therefore, a more general direction of future research could be to examine other bacterial adhesive proteins under constant force to assess whether the ideal + slip bond behavior and the force-independent gateway mechanism is a common trait. This information could provide information on how to better develop antiadhesive therapies for a wide range of bacterial diseases.

References

1. Merkel, R., et al., *Energy landscapes of receptor-ligand bonds explored with dynamic force spectroscopy.* Nature, 1999. **397**(6714): p. 50-3.
2. Yago, T., et al., *Platelet glycoprotein lb alpha forms catch bonds with human WT vWF but not with type 2B von Willebrand disease vWF.* Journal of Clinical Investigation, 2008. **118**(9): p. 3195-3207.
3. Yakovenko, O., et al., *FimH forms catch bonds that are enhanced by mechanical force due to allosteric regulation.* J Biol Chem, 2008. **283**(17): p. 11596-605.
4. Daniels, B.R., B.C. Masi, and D. Wirtz, *Probing single-cell micromechanics in vivo: the microrheology of C. elegans developing embryos.* Biophys J, 2006. **90**(12): p. 4712-9.
5. Smith, S.B., Y. Cui, and C. Bustamante, *Overstretching B-DNA: the elastic response of individual double-stranded and single-stranded DNA molecules.* Science, 1996. **271**(5250): p. 795-9.
6. Block, S.M., L.S. Goldstein, and B.J. Schnapp, *Bead movement by single kinesin molecules studied with optical tweezers.* Nature, 1990. **348**(6299): p. 348-52.
7. Svoboda, K. and S.M. Block, *Force and velocity measured for single kinesin molecules.* Cell, 1994. **77**(5): p. 773-84.
8. Sadler, J.E., *Biochemistry and genetics of von Willebrand factor.* Annu Rev Biochem, 1998. **67**: p. 395-424.
9. Thomas, W., *Catch bonds in adhesion.* Annu Rev Biomed Eng, 2008. **10**: p. 39-57.
10. Foxman, B., *The epidemiology of urinary tract infection.* Nat Rev Urol, 2010. **7**(12): p. 653-60.
11. McGann, P., et al., *Escherichia coli Harboring mcr-1 and blaCTX-M on a Novel IncF Plasmid: First Report of mcr-1 in the United States.* Antimicrob Agents Chemother, 2016. **60**(7): p. 4420-1.
12. Evans, E., *Probing the relation between force--lifetime--and chemistry in single molecular bonds.* Annu Rev Biophys Biomol Struct, 2001. **30**: p. 105-28.
13. Bell, G.I., *Models for the specific adhesion of cells to cells.* Science, 1978. **200**(4342): p. 618-27.
14. Thomas, W., et al., *Catch-bond model derived from allostery explains force-activated bacterial adhesion.* Biophys J, 2006. **90**(3): p. 753-64.
15. Neuman, K.C. and A. Nagy, *Single-molecule force spectroscopy: optical tweezers, magnetic tweezers and atomic force microscopy.* Nat Methods, 2008. **5**(6): p. 491-505.
16. Gourier, C., et al., *A Nanospring Named Erythrocyte. The Biomembrane Force Probe.* Cellular and Molecular Bioengineering, 2008. **1**(4): p. 263-275.
17. Clausen-Schaumann, H., et al., *Force spectroscopy with single bio-molecules.* Curr Opin Chem Biol, 2000. **4**(5): p. 524-30.
18. Evans, E., et al., *Long-lived, high-strength states of ICAM-1 bonds to beta2 integrin, I: lifetimes of bonds to recombinant alphaLbeta2 under force.* Biophys J, 2010. **98**(8): p. 1458-66.
19. Crick, F.H.C. and A.F.W. Hughes, *The Physical Properties of Cytoplasm - a Study by Means of the Magnetic Particle Method .1. Experimental.* Experimental Cell Research, 1950. **1**(1): p. 37-80.
20. Smith, S.B., L. Finzi, and C. Bustamante, *Direct mechanical measurements of the elasticity of single DNA molecules by using magnetic beads.* Science, 1992. **258**(5085): p. 1122-6.
21. De Vlaminck, I., et al., *Highly parallel magnetic tweezers by targeted DNA tethering.* Nano Lett, 2011. **11**(12): p. 5489-93.
22. van Loenhout, M.T., et al., *Non-bias-limited tracking of spherical particles, enabling nanometer resolution at low magnification.* Biophys J, 2012. **102**(10): p. 2362-71.
23. Teulon, J.M., et al., *Single and multiple bonds in (strept)avidin-biotin interactions.* J Mol Recognit, 2011. **24**(3): p. 490-502.

24. Bartsch, T.F., et al., *Detecting sequential bond formation using three-dimensional thermal fluctuation analysis.* Chemphyschem, 2009. **10**(9-10): p. 1541-7.
25. Florin, E.L., V.T. Moy, and H.E. Gaub, *Adhesion forces between individual ligand-receptor pairs.* Science, 1994. **264**(5157): p. 415-7.
26. Yuan, C.B., et al., *Energy landscape of streptavidin-biotin complexes measured by atomic force microscopy.* Biochemistry, 2000. **39**(33): p. 10219-10223.
27. Lo, Y.S., et al., *Specific interactions between biotin and avidin studied by atomic force microscopy using the Poisson statistical analysis method.* Langmuir, 1999. **15**(4): p. 1373-1382.
28. Williams, P.M., *Analytical descriptions of dynamic force spectroscopy: behaviour of multiple connections.* Analytica Chimica Acta, 2003. **479**(1): p. 107-115.
29. Thormann, E., et al., *Dynamic force spectroscopy on soft molecular systems: improved analysis of unbinding spectra with varying linker compliance.* Colloids Surf B Biointerfaces, 2006. **53**(2): p. 149-56.
30. Vanoss, C.J., *Hydrophobicity of Biosurfaces - Origin, Quantitative-Determination and Interaction Energies.* Colloids and Surfaces B-Biointerfaces, 1995. **5**(3-4): p. 91-110.
31. Friddle, R.W., et al., *Single functional group interactions with individual carbon nanotubes.* Nat Nanotechnol, 2007. **2**(11): p. 692-7.
32. Thomas, W.E., et al., *Bacterial adhesion to target cells enhanced by shear force.* Cell, 2002. **109**(7): p. 913-23.
33. Liu, J. and M.J. Butte, *Single molecule labeling of an atomic force microscope cantilever tip.* Appl Phys Lett, 2012. **101**(16): p. 163705.
34. Long, F., et al., *Modification of a single-molecule AFM probe with highly defined surface functionality.* Beilstein J Nanotechnol, 2014. **5**: p. 2122-8.
35. Wang, H., et al., *Functional characterization and atomic force microscopy of a DNA repair protein conjugated to a quantum dot.* Nano Lett, 2008. **8**(6): p. 1631-7.
36. Hoffmann, T. and L. Dougan, *Single molecule force spectroscopy using polyproteins.* Chem Soc Rev, 2012. **41**(14): p. 4781-96.
37. Ott, W., et al., *Single-molecule force spectroscopy on polyproteins and receptor-ligand complexes: The current toolbox.* J Struct Biol, 2017. **197**(1): p. 3-12.
38. Hughes, M.L. and L. Dougan, *The physics of pulling polyproteins: a review of single molecule force spectroscopy using the AFM to study protein unfolding.* Rep Prog Phys, 2016. **79**(7): p. 076601.
39. Scholl, Z.N., Q. Li, and P.E. Marszalek, *Single molecule mechanical manipulation for studying biological properties of proteins, DNA, and sugars.* Wiley Interdiscip Rev Nanomed Nanobiotechnol, 2014. **6**(3): p. 211-29.
40. Sulchek, T.A., et al., *Dynamic force spectroscopy of parallel individual Mucin1-antibody bonds.* Proceedings of the National Academy of Sciences of the United States of America, 2005. **102**(46): p. 16638-16643.
41. Kim, J., et al., *A mechanically stabilized receptor-ligand flex-bond important in the vasculature.* Nature, 2010. **466**(7309): p. 992-U123.
42. Puchner, E.M., et al., *Comparing proteins by their unfolding pattern.* Biophys J, 2008. **95**(1): p. 426-34.
43. Janissen, R., et al., *Invincible DNA tethers: covalent DNA anchoring for enhanced temporal and force stability in magnetic tweezers experiments.* Nucleic Acids Res, 2014. **42**(18): p. e137.
44. Riquelme, M.V., et al., *Optimizing blocking of nonspecific bacterial attachment to impedimetric biosensors.* Sensing and Bio-Sensing Research, 2016. **8**: p. 47-54.

45. Carrion-Vazquez, M., et al., *Mechanical design of proteins studied by single-molecule force spectroscopy and protein engineering.* Prog Biophys Mol Biol, 2000. **74**(1-2): p. 63-91.
46. Tych, K.M., et al., *Single molecule force spectroscopy reveals the temperature-dependent robustness and malleability of a hyperthermophilic protein.* Soft Matter, 2013. **9**(37): p. 9016-9025.
47. Sadler, D.P., et al., *Identification of a mechanical rheostat in the hydrophobic core of protein L.* J Mol Biol, 2009. **393**(1): p. 237-48.
48. Bertz, M., et al., *Structural and mechanical hierarchies in the alpha-crystallin domain dimer of the hyperthermophilic small heat shock protein Hsp16.5.* J Mol Biol, 2010. **400**(5): p. 1046-56.
49. Marszalek, P.E., et al., *Mechanical unfolding intermediates in titin modules.* Nature, 1999. **402**(6757): p. 100-3.
50. Jass, J., et al., *Physical properties of Escherichia coli P pili measured by optical tweezers.* Biophys J, 2004. **87**(6): p. 4271-83.
51. Andersson, M., B.E. Uhlin, and E. Fallman, *The biomechanical properties of E. coli pili for urinary tract attachment reflect the host environment.* Biophys J, 2007. **93**(9): p. 3008-14.
52. Forero, M., et al., *Uncoiling mechanics of Escherichia coli type I fimbriae are optimized for catch bonds.* PLoS Biol, 2006. **4**(9): p. e298.
53. Carrion-Vazquez, M., et al., *The mechanical stability of ubiquitin is linkage dependent.* Nat Struct Biol, 2003. **10**(9): p. 738-43.
54. Furuike, S., T. Ito, and M. Yamazaki, *Mechanical unfolding of single filamin A (ABP-280) molecules detected by atomic force microscopy.* FEBS Lett, 2001. **498**(1): p. 72-5.
55. Khalil, A.S., et al., *Single M13 bacteriophage tethering and stretching.* Proc Natl Acad Sci U S A, 2007. **104**(12): p. 4892-7.
56. Cecconi, C., et al., *DNA molecular handles for single-molecule protein-folding studies by optical tweezers.* Methods Mol Biol, 2011. **749**: p. 255-71.
57. Han, X., et al., *A versatile "multiple fishhooks" approach for the study of ligand-receptor interactions using single-molecule atomic force microscopy.* Langmuir, 2012. **28**(26): p. 10020-5.
58. Valle, F., et al., *A polymeric molecular "handle" for multiple AFM-based single-molecule force measurements.* Angew Chem Int Ed Engl, 2008. **47**(13): p. 2431-4.
59. Wiita, A.P., et al., *Force-dependent chemical kinetics of disulfide bond reduction observed with single-molecule techniques.* Proc Natl Acad Sci U S A, 2006. **103**(19): p. 7222-7.
60. Halvorsen, K., D. Schaak, and W.P. Wong, *Nanoengineering a single-molecule mechanical switch using DNA self-assembly.* Nanotechnology, 2011. **22**(49): p. 494005.
61. Krasnoslobodtsev, A.V., et al., *A flexible nanoarray approach for the assembly and probing of molecular complexes.* Biophys J, 2015. **108**(9): p. 2333-9.
62. Evans, E. and K. Ritchie, *Strength of a weak bond connecting flexible polymer chains.* Biophys J, 1999. **76**(5): p. 2439-47.
63. Friedsam, C., et al., *Dynamic single-molecule force spectroscopy: bond rupture analysis with variable spacer length.* Journal of Physics: Condensed Matter, 2003. **15**(18).
64. Ray, C., J.R. Brown, and B.B. Akhremitchev, *Correction of systematic errors in single-molecule force spectroscopy with polymeric tethers by atomic force microscopy.* J Phys Chem B, 2007. **111**(8): p. 1963-74.
65. Walton, E.B., S. Lee, and K.J. Van Vliet, *Extending Bell's model: how force transducer stiffness alters measured unbinding forces and kinetics of molecular complexes.* Biophys J, 2008. **94**(7): p. 2621-30.
66. Getfert, S. and P. Reimann, *Hidden multiple bond effects in dynamic force spectroscopy.* Biophys J, 2012. **102**(5): p. 1184-93.

67. Mayyas, E., et al., *Dissociation Kinetics of an Enzyme-Inhibitor System Using Single-Molecule Force Measurements.* Biomacromolecules, 2010. **11**(12): p. 3352-3358.
68. Wong, J., A. Chilkoti, and V.T. Moy, *Direct force measurements of the streptavidin-biotin interaction.* Biomol Eng, 1999. **16**(1-4): p. 45-55.
69. Lo, Y.S., J. Simons, and T.P. Beebe, *Temperature dependence of the biotin-avidin bond-rupture force studied by atomic force microscopy.* Journal of Physical Chemistry B, 2002. **106**(38): p. 9847-9852.
70. Stevens, F., et al., *Computer modeling of atomic force microscopy force measurements: Comparisons of Poisson, histogram, and continuum methods.* Langmuir, 1999. **15**(1): p. 207-213.
71. Guo, S., et al., *Effects of multiple-bond ruptures on kinetic parameters extracted from force spectroscopy measurements: Revisiting biotin-streptavidin interactions.* Biophysical Journal, 2008. **95**(8): p. 3964-3976.
72. Erdmann, T., et al., *Dynamic force spectroscopy on multiple bonds: Experiments and model.* Epl, 2008. **81**(4).
73. Sun, L., et al., *Effect of loading conditions on the dissociation behaviour of catch bond clusters.* J R Soc Interface, 2012. **9**(70): p. 928-37.
74. Huang, W., et al., *Dimerization of Cell-Adhesion Molecules Can Increase Their Binding Strength.* Langmuir, 2017. **33**(6): p. 1398-1404.
75. Lee, G.U., D.A. Kidwell, and R.J. Colton, *Sensing Discrete Streptavidin Biotin Interactions with Atomic-Force Microscopy.* Langmuir, 1994. **10**(2): p. 354-357.
76. Piramowicz, M.D., et al., *Dynamic force measurements of avidin-biotin and streptavdin-biotin interactions using AFM.* Acta Biochimica Polonica, 2006. **53**(1): p. 93-100.
77. Williams, P.M., et al., *On the dynamic behaviour of the forced dissociation of ligand-receptor pairs.* Journal of the Chemical Society-Perkin Transactions 2, 2000(1): p. 5-8.
78. Rico, F. and V.T. Moy, *Energy landscape roughness of the streptavidin-biotin interaction.* Journal of Molecular Recognition, 2007. **20**(6): p. 495-501.
79. Pincet, F. and J. Husson, *The solution to the streptavidin-biotin paradox: The influence of history on the strength of single molecular bonds.* Biophysical Journal, 2005. **89**(6): p. 4374-4381.
80. Zhang, X. and V.T. Moy, *Cooperative adhesion of ligand-receptor bonds.* Biophys Chem, 2003. **104**(1): p. 271-8.
81. Moy, V.T., E.L. Florin, and H.E. Gaub, *Intermolecular forces and energies between ligands and receptors.* Science, 1994. **266**(5183): p. 257-9.
82. Panhorst, M., et al., *Sensitive bondforce measurements of ligand-receptor pairs with magnetic beads.* Biosensors & Bioelectronics, 2005. **20**(8): p. 1685-1689.
83. Patel, A.B., et al., *Influence of architecture on the kinetic stability of molecular assemblies.* Journal of the American Chemical Society, 2004. **126**(5): p. 1318-1319.
84. Jeney, S., et al., *Monitoring ligand-receptor interactions by photonic force microscopy.* Nanotechnology, 2010. **21**(25).
85. Ray, C., et al., *Kinetic parameters from detection probability in single molecule force spectroscopy.* Langmuir, 2010. **26**(14): p. 11951-7.
86. Ota, T., T. Sugiura, and S. Kawata, *Rupture force measurement of biotin-streptavidin bonds using optical trapping.* Applied Physics Letters, 2005. **87**(4).
87. Taninaka, A., O. Takeuchi, and H. Shigekawa, *Reconsideration of Dynamic Force Spectroscopy Analysis of Streptavidin-Biotin Interactions.* International Journal of Molecular Sciences, 2010. **11**(5): p. 2134-2151.
88. De Vlaminck, I. and C. Dekker, *Recent advances in magnetic tweezers.* Annu Rev Biophys, 2012. **41**: p. 453-72.

89. Ribeck, N. and O.A. Saleh, *Multiplexed single-molecule measurements with magnetic tweezers.* Rev Sci Instrum, 2008. **79**(9): p. 094301.
90. Snook, J.H. and W.H. Guilford, *A High-Throughput Technique Reveals the Load- and Site Density-Dependent Kinetics of E-Selectin.* Cell Mol Bioeng, 2012. **5**(4): p. 493-503.
91. Zhang, Z. and C.H. Menq, *Three-dimensional particle tracking with subnanometer resolution using off-focus images.* Appl Opt, 2008. **47**(13): p. 2361-70.
92. Cnossen, J.P., D. Dulin, and N.H. Dekker, *An optimized software framework for real-time, high-throughput tracking of spherical beads.* Rev Sci Instrum, 2014. **85**(10): p. 103712.
93. Gosse, C. and V. Croquette, *Magnetic tweezers: micromanipulation and force measurement at the molecular level.* Biophys J, 2002. **82**(6): p. 3314-29.
94. Kauert, D.J., et al., *Direct mechanical measurements reveal the material properties of three-dimensional DNA origami.* Nano Lett, 2011. **11**(12): p. 5558-63.
95. Kruithof, M., et al., *Subpiconewton dynamic force spectroscopy using magnetic tweezers.* Biophys J, 2008. **94**(6): p. 2343-8.
96. McAndrew, C.P., et al., *Simple horizontal magnetic tweezers for micromanipulation of single DNA molecules and DNA-protein complexes.* Biotechniques, 2016. **60**(1): p. 21-7.
97. Min, D., et al., *Mechanical unzipping and rezipping of a single SNARE complex reveals hysteresis as a force-generating mechanism.* Nat Commun, 2013. **4**: p. 1705.
98. Yang, Y., et al., *Microrheology of highly crosslinked microtubule networks is dominated by force-induced crosslinker unbinding.* Soft Matter, 2013. **9**(2): p. 383-393.
99. Yao, M., et al., *Mechanical activation of vinculin binding to talin locks talin in an unfolded conformation.* Sci Rep, 2014. **4**: p. 4610.
100. Ishikawa, Y. and S. Chikazumi, *Design of High Power Electromagnets.* Japanese Journal of Applied Physics, 1962. **1**(3): p. 155-173.
101. Ganatos, P., R. Pfeffer, and S. Weinbaum, *A Strong Interaction Theory for the Creeping Motion of a Sphere between Plane Parallel Boundaries .2. Parallel Motion.* Journal of Fluid Mechanics, 1980. **99**(Aug): p. 755-783.
102. Maude, A., *End Effects in a falling-sphere viscometer.* British Journal of Applied Physics, 1961. **12**: p. 293-295.
103. Whitfield, M.J., J.P. Luo, and W.E. Thomas, *Yielding elastic tethers stabilize robust cell adhesion.* PLoS Comput Biol, 2014. **10**(12): p. e1003971.
104. Whitfield, M. and W.E. Thomas, *A Nanoadhesive Composed of Receptor-Ligand Bonds.* Journal of Adhesion, 2011. **87**(5): p. 427-446.
105. Whitfield, M., T. Ghose, and W. Thomas, *Shear-stabilized rolling behavior of E. coli examined with simulations.* Biophys J, 2010. **99**(8): p. 2470-8.
106. Berg-Sorensen, K. and H. Flyvbjerg, *Power spectrum analysis for optical tweezers.* Review of Scientific Instruments, 2004. **75**(3): p. 594-612.
107. Zhang, X., et al., *Mechanoenzymatic cleavage of the ultralarge vascular protein von Willebrand factor.* Science, 2009. **324**(5932): p. 1330-4.
108. Tchesnokova, V., et al., *Integrin-like allosteric properties of the catch bond-forming FimH adhesin of Escherichia coli.* J Biol Chem, 2008. **283**(12): p. 7823-33.
109. Marshall, B.T., et al., *Direct observation of catch bonds involving cell-adhesion molecules.* Nature, 2003. **423**(6936): p. 190-193.
110. Sarangapani, K.K., et al., *Low force decelerates L-selectin dissociation from P-selectin glycoprotein ligand-1 and endoglycan.* Journal of Biological Chemistry, 2004. **279**(3): p. 2291-2298.

111. Snook, J.H. and W.H. Guilford, *The Effects of Load on E-Selectin Bond Rupture and Bond Formation.* Cellular and Molecular Bioengineering, 2010. **3**(2): p. 128-138.
112. Chen, W., et al., *Observing force-regulated conformational changes and ligand dissociation from a single integrin on cells.* Journal of Cell Biology, 2012. **199**(3): p. 497-512.
113. Chen, W., J.Z. Lou, and C. Zhu, *Forcing Switch from Short- to Intermediate- and Long-lived States of the alpha A Domain Generates LFA-1/ICAM-1 Catch Bonds.* Journal of Biological Chemistry, 2010. **285**(46): p. 35967-35978.
114. Kong, F., et al., *Demonstration of catch bonds between an integrin and its ligand.* Journal of Cell Biology, 2009. **185**(7): p. 1275-1284.
115. Kong, F., et al., *Cyclic Mechanical Reinforcement of Integrin-Ligand Interactions.* Molecular Cell, 2013. **49**(6): p. 1060-1068.
116. Manibog, K., et al., *Resolving the molecular mechanism of cadherin catch bond formation.* Nature Communications, 2014. **5**.
117. Rakshit, S., et al., *Ideal, catch, and slip bonds in cadherin adhesion.* Proc Natl Acad Sci U S A, 2012. **109**(46): p. 18815-20.
118. Liu, B.Y., et al., *Accumulation of Dynamic Catch Bonds between TCR and Agonist Peptide-MHC Triggers T Cell Signaling.* Cell, 2014. **157**(2): p. 357-368.
119. Litvinov, R.I. and J.W. Weisel, *Shear strengthens fibrin: the knob-hole interactions display 'catch-slip' kinetics.* Journal of Thrombosis and Haemostasis, 2013. **11**(10): p. 1933-1935.
120. Karlowsky, J.A., et al., *Trends in antimicrobial resistance among urinary tract infection isolates of Escherichia coli from female outpatients in the United States.* Antimicrob Agents Chemother, 2002. **46**(8): p. 2540-5.
121. Schito, G.C., et al., *The ARESC study: an international survey on the antimicrobial resistance of pathogens involved in uncomplicated urinary tract infections.* Int J Antimicrob Agents, 2009. **34**(5): p. 407-13.
122. Zhanel, G.G., et al., *Antibiotic resistance in outpatient urinary isolates: final results from the North American Urinary Tract Infection Collaborative Alliance (NAUTICA).* Int J Antimicrob Agents, 2005. **26**(5): p. 380-8.
123. Cheever, K., *Brunner & Suddarth's textbook of medical-surgical nursing*. 2010, Philadelphia: Wolters Kluwer Health/Lippincott Williams & Wilkins.
124. Le Trong, I., et al., *Donor strand exchange and conformational changes during E. coli fimbrial formation.* J Struct Biol, 2010. **172**(3): p. 380-8.
125. Astrof, N.S., et al., *Importance of force linkage in mechanochemistry of adhesion receptors.* Biochemistry, 2006. **45**(50): p. 15020-15028.
126. Boettiger, D., *Using force to visualize conformational activation of integrins.* Journal of Cell Biology, 2012. **199**(3): p. 423-424.
127. Federici, A.B., et al., *Clinical and molecular predictors of thrombocytopenia and risk of bleeding in patients with vonWillebrand disease type 2B: a cohort study of 67 patients.* Blood, 2009. **113**(3): p. 526-534.
128. Grzymajlo, K., et al., *The high-adhesive properties of the FimH adhesin of Salmonella enterica serovar Enteritidis are determined by a single F118S substitution.* Microbiology, 2010. **156**(Pt 6): p. 1738-48.
129. Hynes, R.O., *Integrins: Bidirectional, allosteric signaling machines.* Cell, 2002. **110**(6): p. 673-687.
130. Kisiela, D.I., et al., *Allosteric catch bond properties of the FimH adhesin from Salmonella enterica serovar Typhimurium.* J Biol Chem, 2011. **286**(44): p. 38136-47.

131. Liu, Y., et al., *Tight Conformational Coupling between the Domains of the Enterotoxigenic Escherichia coli Fimbrial Adhesin CfaE Regulates Binding State Transition.* Journal of Biological Chemistry, 2013. **288**(14): p. 9993-10001.
132. Lou, J.Z., et al., *Flow-enhanced adhesion regulated by a selectin interdomain hinge.* Journal of Cell Biology, 2006. **174**(7): p. 1107-1117.
133. Phan, U.T., T. T Waldron, and T.A. Springer, *Remodeling of the lectin-EGF-like domain interface in P- and L-selectin increases adhesiveness and shear resistance under hydrodynamic force.* Nature Immunology, 2006. **7**(8): p. 883-889.
134. Springer, T.A., *Structural basis for selectin mechanochemistry.* Proceedings of the National Academy of Sciences of the United States of America, 2009. **106**(1): p. 91-96.
135. Stahlhut, S.G., et al., *Comparative structure-function analysis of mannose-specific FimH adhesins from Klebsiella pneumoniae and Escherichia coli.* J Bacteriol, 2009. **191**(21): p. 6592-601.
136. Tchesnokova, V., et al., *Shear-enhanced binding of intestinal colonization factor antigen I of enterotoxigenic Escherichia coli.* Mol Microbiol, 2010. **76**(2): p. 489-502.
137. Thomas, W.E., *Mechanochemistry of receptor-ligand bonds.* Current Opinion in Structural Biology, 2009. **19**(1): p. 50-55.
138. Ulrichts, H., et al., *A monoclonal antibody directed against human von Willebrand factor induces type 2B-like alterations.* Journal of Thrombosis and Haemostasis, 2004. **2**(9): p. 1622-1628.
139. Vanhoorelbeke, K., et al., *The Novel S527F Mutation in the Integrin beta 3 Chain Induces a High Affinity alpha IIb beta 3 Receptor by Hindering Adoption of the Bent Conformation.* Journal of Biological Chemistry, 2009. **284**(22): p. 14914-14920.
140. Waldron, T.T. and T.A. Springer, *Transmission of allostery through the lectin domain in selectin-mediated cell adhesion.* Proceedings of the National Academy of Sciences of the United States of America, 2009. **106**(1): p. 85-90.
141. Xiang, X., et al., *Structural Basis and Kinetics of Force-Induced Conformational Changes of an alpha A Domain-Containing Integrin.* Plos One, 2011. **6**(11).
142. Fernandes, H., et al., *Structural and functional aspects of PR-10 proteins.* Febs Journal, 2013. **280**(5): p. 1169-1199.
143. Harel, M., et al., *Quaternary Ligand-Binding to Aromatic Residues in the Active-Site Gorge of Acetylcholinesterase.* Proceedings of the National Academy of Sciences of the United States of America, 1993. **90**(19): p. 9031-9035.
144. Joseph, D., G.A. Petsko, and M. Karplus, *Anatomy of a Conformational Change - Hinged Lid Motion of the Triosephosphate Isomerase Loop.* Science, 1990. **249**(4975): p. 1425-1428.
145. Li, P.L., et al., *Internal dynamics control activation and activity of the autoinhibited Vav DH domain.* Nature Structural & Molecular Biology, 2008. **15**(6): p. 613-618.
146. Melcher, K., et al., *A gate-latch-lock mechanism for hormone signalling by abscisic acid receptors.* Nature, 2009. **462**(7273): p. 602-U72.
147. Miller, B.G., et al., *Anatomy of a proficient enzyme: The structure of orotidine 5 '-monophosphate decarboxylase in the presence and absence of a potential transition state analog.* Proceedings of the National Academy of Sciences of the United States of America, 2000. **97**(5): p. 2011-2016.
148. Murase, K., et al., *Gibberellin-induced DELLA recognition by the gibberellin receptor GID1.* Nature, 2008. **456**(7221): p. 459-U15.
149. Russell, R.J., et al., *The structure of H5N1 avian influenza neuraminidase suggests new opportunities for drug design.* Nature, 2006. **443**(7107): p. 45-49.
150. Seo, M.H., et al., *Protein conformational dynamics dictate the binding affinity for a ligand.* Nature Communications, 2014. **5**.

151. Unal, H., et al., *Ligand-specific Conformation of Extracellular Loop-2 in the Angiotensin II Type 1 Receptor.* Journal of Biological Chemistry, 2010. **285**(21): p. 16341-16350.
152. Whittier, S.K., A.C. Hengge, and J.P. Loria, *Conformational Motions Regulate Phosphoryl Transfer in Related Protein Tyrosine Phosphatases.* Science, 2013. **341**(6148): p. 899-903.
153. Wolf-Watz, M., et al., *Linkage between dynamics and catalysis in a thermophilic-mesophilic enzyme pair.* Nature Structural & Molecular Biology, 2004. **11**(10): p. 945-949.
154. Boehr, D.D., R. Nussinov, and P.E. Wright, *The role of dynamic conformational ensembles in biomolecular recognition (vol 5, pg 789, 2009).* Nature Chemical Biology, 2009. **5**(12): p. 954-954.
155. Carroll, M.J., et al., *Evidence for dynamics in proteins as a mechanism for ligand dissociation.* Nature Chemical Biology, 2012. **8**(3): p. 246-252.
156. Brooks, D.E., et al., *Involvement of the MN blood group antigen in shear-enhanced hemagglutination induced by the Escherichia coli F41 adhesin.* Infect Immun, 1989. **57**(2): p. 377-83.
157. Ding, A.M., et al., *Shear-enhanced oral microbial adhesion.* Appl Environ Microbiol, 2010. **76**(4): p. 1294-7.
158. Lecuyer, S., et al., *Shear stress increases the residence time of adhesion of Pseudomonas aeruginosa.* Biophys J, 2011. **100**(2): p. 341-50.
159. Li, Z.J., N. Mohamed, and J.M. Ross, *Shear stress affects the kinetics of Staphylococcus aureus adhesion to collagen.* Biotechnol Prog, 2000. **16**(6): p. 1086-90.
160. Nilsson, L.M., et al., *Catch bond-mediated adhesion without a shear threshold: trimannose versus monomannose interactions with the FimH adhesin of Escherichia coli.* J Biol Chem, 2006. **281**(24): p. 16656-63.
161. Thomas, W.E., et al., *Shear-dependent 'stick-and-roll' adhesion of type 1 fimbriated Escherichia coli.* Mol Microbiol, 2004. **53**(5): p. 1545-57.
162. Weaver, W.M., et al., *The effects of shear stress on isolated receptor-ligand interactions of Staphylococcus epidermidis and human plasma fibrinogen using molecularly patterned microfluidics.* Lab Chip, 2011. **11**(5): p. 883-9.
163. Alon, R. and S. Feigelson, *From rolling to arrest on blood vessels: leukocyte tap dancing on endothelial integrin ligands and chemokines at sub-second contacts.* Seminars in Immunology, 2002. **14**(2): p. 93-104.
164. Litvinov, R.I., et al., *Dissociation of Bimolecular alpha llb beta 3-Fibrinogen Complex under a Constant Tensile Force.* Biophysical Journal, 2011. **100**(1): p. 165-173.
165. Litvinov, R.I., et al., *Resolving Two-dimensional Kinetics of the Integrin alpha IIb beta 3-Fibrinogen Interactions Using Binding-Unbinding Correlation Spectroscopy.* Journal of Biological Chemistry, 2012. **287**(42): p. 35275-35285.
166. Takamatsu, D., et al., *Binding of the Streptococcus gordonii surface glycoproteins GspB and Hsa to specific carbohydrate structures on platelet membrane glycoprotein Ibalpha.* Mol Microbiol, 2005. **58**(2): p. 380-92.
167. Rodriguez, V.B., et al., *Allosteric coupling in the bacterial adhesive protein FimH.* J Biol Chem, 2013. **288**(33): p. 24128-39.
168. Sauer, M.M., et al., *Catch-bond mechanism of the bacterial adhesin FimH.* Nat Commun, 2016. **7**: p. 10738.
169. Nilsson, L.M., et al., *Beyond induced-fit receptor-ligand interactions: structural changes that can significantly extend bond lifetimes.* Structure, 2008. **16**(7): p. 1047-58.
170. Jungmann, R., et al., *DNA origami-based nanoribbons: assembly, length distribution, and twist.* Nanotechnology, 2011. **22**(27): p. 275301.

171. Kocabey, S., et al., *Membrane-assisted growth of DNA origami nanostructure arrays.* ACS Nano, 2015. **9**(4): p. 3530-9.

172. Liu, W., et al., *Crystalline two-dimensional DNA-origami arrays.* Angew Chem Int Ed Engl, 2011. **50**(1): p. 264-7.

173. Rajendran, A., M. Endo, and H. Sugiyama, *Single-molecule analysis using DNA origami.* Angew Chem Int Ed Engl, 2012. **51**(4): p. 874-90.

174. Rinker, S., et al., *Self-assembled DNA nanostructures for distance-dependent multivalent ligand-protein binding.* Nat Nanotechnol, 2008. **3**(7): p. 418-22.

175. Zhao, Z., Y. Liu, and H. Yan, *Organizing DNA origami tiles into larger structures using preformed scaffold frames.* Nano Lett, 2011. **11**(7): p. 2997-3002.

Curriculum Vitae
Keith Charles Johnson

Experience

University of Washington Seattle, WA
Dates: June 2011 – April 2017
Job Title: Research Assistant

Designed and optimized an instrument that massively improved the throughput of single molecule force measurements. This involved CAD modeling of hardware components, writing software to provide synchronous control of various devices, development of an algorithm that determines the three-dimensional position of small particles with sub-nanometer resolution, and optimizing experimental wet-bench protocols for consistent and reliable data acquisition. Currently using this instrument to characterize the force dependence of bacterial binding to epithelial cells. Also helped write a stochastic simulation that models the binding behavior of *E. coli* bacteria.

Edmonds-Woodway H.S. Edmonds, WA
Dates: July 2015-current
Job Title: Assistant Cross Country Coach

Assisted in the training and management of the boys and girls varsity cross country teams. This included communicating training philosophies, assisting in conflict resolution within the teams, and coordinating the logistics of cross country meets.

University of Washington Seattle, WA
Dates: Jan 2010 – June 2011
Job Title: Research Assistant

Directed experiments determining heat dissipation in a composite panel. This involved the use of thermocouples and a thermographic camera that captured infrared images. Analysis of these temperatures and the resulting heat losses were determined using inverse numerical methods and finite element simulations using MATLAB and COMSOL Multiphysics.

Esco Corporation Portland, OR
Dates: Apr 2007 – Sep 2009
Job Title: Design Engineer

Worked as part of the Construction Expendables Optimization Team designing, optimizing, testing, and problem-solving cast steel tooth and adapter systems for large earth moving equipment. Lead a team of engineers to reduce crack occurrence in manufacturing plants using FEA and CFD analysis tools.

Two full-time, six-month internships for the Multiple Engineering Cooperative Program (MECOP). Internship details below.

Intel Corporation: Hillsboro, OR
Dates: Apr 2006 – Sep 2006
Job Title: Operations Manager

Helped manage the fabrication facilities where CPU's, chip sets, and memory are manufactured. Dealt with machine, personnel, and product strategy issues as they occurred. Participated on several project teams concerned with the implementation of new products and programs.

Freightliner LLC: **Portland, OR**
Dates: Apr 2005 – Sep 2005
Job Title: Technical Market Analyst
Used Freightliner sales data to create reports on sales and technical trends within the trucking market. This information was used to develop sales strategy and ideas for future truck power trains.

Education

University of Washington **Seattle, WA**
Degree: Doctor of Philosophy: Mechanical Engineering
Date of Graduation: 4/31/2017
GPA: 3.73

University of Washington **Seattle, WA**
Degree: Master of Science: Mechanical Engineering
Date of Graduation: 6/12/2011
GPA: 3.71

Oregon State University **Corvallis, OR**
Degree: Bachelor of Science: Mechanical Engineering
Date of Graduation: 3/23/2007
GPA: 3.14

Professional Qualifications

Proficient with wet lab techniques, NX Unigraphics, SolidWorks, MATLAB, COMSOL, LabView, LaTeX, Microsoft Office applications
Experience with C++, ProE, Python, Mathematica
Successfully passed the Fundamentals of Engineering Examination

Publications

Emery, A.F. and K.C. Johnson, *Practical considerations when using sparse grids with Bayesian inference for parameter estimation.* Inverse Problems in Science and Engineering, 2012. **20**(5): p. 591-608.

Interests

Reading, running, swimming, soccer, traveling.